Pacific Interannual and Interdecadal Equatorial Variability in a 1000-Yr Simulation of the CSIRO Coupled General Circulation Model*

DANIEL J. VIMONT AND DAVID S. BATTISTI

Department of Atmospheric Sciences, University of Washington, Seattle, Washington

ANTHONY C. HIRST

CRC for Southern Hemisphere Meteorology, CSIRO Division of Atmospheric Research, Aspendale, Victoria, Australia

(Manuscript received 20 February 2001, in final form 20 June 2001)

ABSTRACT

The structure and evolution of, and the mechanisms responsible for, interannual and decadal equatorial variability in a 1000-yr simulation of the Commonwealth Scientific and Industrial Research Organisation (CSIRO) coupled general circulation model are examined. Principal component analysis is applied to the 0–270-m integrated heat content from the model to determine dominant modes of variability. The leading mode of unfiltered variability (annual) is best described by an AR2 null hypothesis with an implied periodic timescale of 6–10 yr. Spatial structures of the leading empirical modes of interannual (10-yr high-pass filtered) and decadal (9-yr low-pass filtered) variability closely resemble observations of interannual ENSO, and decadal ENSO-like variability. The amplitude of tropical SST anomalies is too small by a factor of 2–3 on interannual timescales, but is close to that observed for decadal timescales.

For interannual timescales, an equatorial heat budget analysis shows a positive feedback between zonal wind stress anomalies, thermocline depth, and SST anomalies along the equator: the so-called Bjerkness feedback. A delayed negative feedback is provided by westward-propagating signals (produced by the same tropical zonal wind stress anomalies) that reflect off the western boundary, and counter the local positive feedback. Combined with the results from the spectral analysis, the heat budget analysis shows that the processes responsible for the interannual variability are consistent with the delayed oscillator mechanism for ENSO; an emerging warm or cold ENSO event contains within it the seeds of its own destruction via the delayed, restoring ocean dynamics.

The decadal heat budget analysis shows the same positive feedback that exists on interannual timescales. However, unlike interannual timescales, for decadal timescales there is little evidence of a delayed negative feedback provided by signals reflecting off the western boundary. The lack of a negative feedback is partially explained by the different meridional structure of interannual and decadal zonal wind stress anomalies. Anomalies associated with the decadal variability decay by numerous processes, including strong surface heat fluxes, and advection by the equatorial undercurrent.

1. Introduction

Observed variability in the Pacific has been shown to be dominated by changes in the Tropics for timescales ranging from interannual to interdecadal (Zhang et al. 1997). For interannual timescales, the El Niño–Southern Oscillation (ENSO) phenomenon dominates variability not only in the tropical Pacific, but globally (see Wallace et al. 1998, for an overview of observed variability associated with ENSO). The mechanism responsible for the existence and evolution of ENSO is relatively well understood (see Neelin et al. 1998, for a review). For decadal to interdecadal timescales, numerous studies have shown that Pacific, and global, variability is dominated by a phenomenon with spatial characteristics that closely resemble ENSO (Yukimoto et al. 1996; Zhang et al. 1997; Knutson and Manabe 1998; Garreaud and Battisti 1999; Lau and Weng 1999). Mantua et al. (1997) recover the same features of ENSO-like decadal variability in their analysis of sea surface temperature (SST) in the North Pacific, and dub the phenomenon the Pacific Decadal Oscillation.

It has been shown that the so-called delayed oscillator mechanism is a major contributor to interannual variability in the tropical Pacific (Schopf and Suarez 1988; Battisti and Hirst 1989; Mantua and Battisti 1994; and reviews by Battisti and Sarachik 1995; Neelin et al. 1998). In the central and eastern equatorial Pacific, cou-

* Joint Institute for the Study of the Atmosphere and Ocean Contribution Number 805.

Corresponding author address: Daniel J. Vimont, Department of Atmospheric Sciences, University of Washington, Box 354235, Seattle, WA 98195-4235.
E-mail: dvimont@atmos.washington.edu

pled equatorial dynamics provide a positive feedback between zonal wind stress, thermocline depth, and SST, which governs the development of an ENSO event. This positive feedback is typically referred to as the ''Bjerkness feedback.''[1] At the same time, the zonal wind stress anomalies force freely propagating oceanic signals in the western equatorial Pacific that reflect off the western ocean boundary, and counter the local positive feedback some time later. The negative feedback is referred to as the ''ocean memory.'' Thus, the delayed oscillator mechanism may be interpreted as the statement that an interannual ENSO event, once initiated, contains not only a mechanism through which it amplifies, but also the seeds of its own destruction. The delayed oscillator mechanism has been shown to exist in observations (Mantua and Battisti 1994), and in numerous models of differing complexity (see Neelin et al. 1998, for a review), including some coarse-resolution coupled general circulation models (CGCMs); (e.g., Moore 1995; Knutson et al. 1997; Timmermann et al. 1999).

The role of stochastic forcing in the delayed oscillator mechanism is a subject of recent debate. In the first intermediate coupled models (ICMs) of ENSO (Zebiak and Cane 1987; Battisti 1988; Schopf and Suarez 1988), interannual variability is sustained without stochastic forcing. In these models, an ENSO event is initiated by the Rossby waves associated with the previous (opposite polarity) event's negative ocean memory feedback. ENSO in these models is the leading linearly unstable eigenmode of the coupled system, where exponential growth is curbed by nonlinearity. Naturally, stochastic forcing may be added to these models, but its presence is not essential in sustaining interannual variability. In a contrasting regime, Thompson and Battisti (2001) have linearized the Battisti (1988) ICM, and shown that, without stochastic forcing, the leading Floquet mode (the ENSO, or delayed oscillator mode) supports decaying interannual oscillations. In their model, interannual variability may be sustained by adding stochastic forcing. In each of these ICMs, the delayed oscillator mechanism governs the evolution of an individual ENSO event. However, in the case of the unstable regime the mechanism responsible for sustaining the variability (and irregularity) of ENSO is the ENSO mode itself; in the stable regime irregularity and variance are largely due to the stochastic forcing. While a strict determination of a specific regime in which the present model's interannual variability resides is beyond the scope of this study, the characteristics of interannual variability in these ICMs will be compared with the interannual variability in the present model.

In contrast to interannual variability, there is no consensus on the mechanism responsible for decadal to interdecadal variability in the Pacific. This disagreement is partly due to a paucity of observations. In this respect, long simulations with viable coupled models provide a unique and crucial framework for studying the mechanisms responsible for decadal and interdecadal variability in the Pacific. Indeed, based on the results from different modeling studies, numerous mechanisms have been hypothesized with which to explain the existence of decadal ENSO-like variability in the Pacific (see Latif 1998; Davis et al. 2000, for reviews). While many of these mechanisms involve very different physical phenomena, the similarity between the spatial structure of interannual and decadal variability in the tropical Pacific has led to a default hypothesis for decadal variability that typically invokes a variant of the delayed oscillator mechanism. As this mechanism dominates variability on interannual timescales, it is likely that it may also give rise to decadal variability. For instance, it is possible that decadal ENSO-like variability is simply a residual of a stochastically forced, or chaotic, ENSO cycle (e.g., Chang et al. 1996; Thompson and Battisti 2001). In this case, the decadal ENSO-like variability exists because of stochastic forcing, or nonlinearity in the tropical coupled dynamics. Other studies posit that tropical decadal variability is governed by low-frequency delayed oscillator physics, where the longer timescale of the variability is hypothesized to be due to a poleward displacement of the wind stress curl in the central Pacific (relative to that associated with the interannual ENSO phenomenon; Yukimoto et al. 1996; Knutson and Manabe 1998), and, hence, a poleward displacement of the restoring oceanic Rossby waves (see also McCreary 1983; Kirtman 1997).

A number of more exotic explanations of decadal variability in the Tropics have been proposed involving different physical mechanisms than those operating on interannual timescales. In contrast to the default hypothesis that coupled dynamics is responsible for tropical variability, Kitoh et al. (1999) find a dominant ENSO-like spatial structure of variability in a coupled atmosphere–mixed layer ocean model. This variability exists through atmosphere and ocean feedbacks that are communicated via changes in the short-wave and latent surface fluxes due to changes in cloudiness and surface wind speed, respectively. More recent studies have suggested that an oceanic pathway between the extratropics and Tropics might give rise to decadal tropical variability. Midlatitude atmospheric variability forces signals in the midlatitude and subtropical oceans, which may reach the Tropics through advection along mean isopycnals (Liu et al. 1994; Gu and Philander 1997; Deser et al. 1996), or through wave propagation (Lysne et al. 1997). This mechanism may exist regardless of whether the midlatitude atmospheric variability is teleconnected with, or independent of, the tropical forcing. In examining these hypotheses, Schneider et al. (1999) and Pierce et al. (2000) show that ocean temperature anomalies arriving in the Tropics via oceanic pathways likely originate in the sub-

[1] The Bjerkness feedback in models includes a rich mix of processes that contribute to changing SST, including upwelling changes and horizontal advection. See, e.g., Zebiak (1985) or Battisti (1988).

tropics (equatorward of 18°N) rather than the midlatitudes. Furthermore, Nonaka et al. (1999) find that temperature anomalies are damped by isopycnal mixing as they propagate equatorward. Finally, several studies argue from the results of CGCMs that the tropical decadal variability may be a passive response to intrinsic midlatitude variability that extends deep enough into the subtropics to affect the evolution of the tropical Pacific coupled system (Barnett et al. 1999; Pierce et al. 2000; Vimont et al. 2001).

Bearing in mind the importance of a realistic simulation of climate variability by global climate models, and the utility of a lengthy model integration, Walland et al. (2000) analyzed the structure of decadal variability in the Commonwealth Scientific and Industrial Research Organisation (CSIRO) CGCM. They found that the temperature and precipitation fields associated with the simulated Pacific decadal variability are ENSO-like (Zhang et al. 1997), and match observations quite well. This study builds on the results of Walland et al. (2000) by extending their analysis to include both interannual and decadal timescales, and other climate variables [e.g., heat content, sea level pressure (SLP), wind stress]. Additionally, through analyzing key processes in the tropical Pacific, we seek to identify mechanisms responsible for the evolution of the simulated interannual ENSO and decadal ENSO-like variability.

This study is organized as follows. Section 2 briefly describes the CSIRO CGCM, and the simulation used. A description of the spatial and temporal structure of simulated Pacific variability is presented in section 3. Based on the conclusions from section 3, the data are temporally filtered to investigate the mechanisms causing interannual and decadal variability in the CSIRO model. In section 4, the evolution and dynamics of modeled tropical Pacific interannual variability are discussed. The discussion of interannual variability provides a reference with which to compare the evolution and dynamics of the simulated tropical Pacific decadal variability in section 5. Section 6 provides a brief summary and discussion of the findings.

2. Model and data

In this study we will use output from the CSIRO global climate model. The coupled model includes atmosphere, ocean, land, and sea-ice model components. The atmospheric component of the CSIRO climate model is spectral, with rhomboidal truncation at 21 wavenumbers (R21). This corresponds to a physical grid of about 3.2° latitude by 5.6° longitude. The vertical dimension is represented by nine sigma levels. The model has an annual and diurnal cycle, and is integrated with a time step of 30 min. The sea-ice model is described in O'Farrell (1998). A more complete description of the atmospheric model, and a description of the land surface model can be found in Gordon and O'Farrell (1997).

The atmosphere, land, and sea-ice models are coupled to a dynamic ocean model that is based on the Bryan–Cox code (Cox 1984). The ocean model's horizontal resolution matches the atmospheric model's physical grid (3.2° lat by 5.6° long), and has 21 vertical levels. While the spatial resolution is too coarse to simulate finescale details of equatorial waves, the general physics of large-scale ocean basin adjustment is still captured in the model. In accord with the results of Ng and Hsieh (1994) and Tett (1995), we interpret the coarse model resolution as having an artificially increased damping on tropical variability. This interpretation is supported by the findings of this study. The ocean's interior vertical diffusivity is calculated as a function of stratification (Gargett 1984), though with a default minimum set at 0.3 $cm^2\ s^{-1}$. To simulate a surface mixed layer, this default minimum is raised to 20 $cm^2\ s^{-1}$ between levels 1 and 2, and 1 $cm^2\ s^{-1}$ between levels 2 and 3. The effect of oceanic mesoscale eddies on tracer transport is parameterized using the scheme of Gent and McWilliams (1990). A more complete description of the ocean model is provided in Hirst et al. (2000).

The coupled integration was performed at CSIRO. The ocean and atmosphere general circulation models (GCMs) were spun up (the spinup procedure is described in Gordon and O'Farrell 1997), and then coupled. An adjustment is made to the surface heat, freshwater, and momentum fluxes between the ocean model and the atmosphere or sea-ice model, and the SST and sea surface salinity in the upper level of the ocean model are adjusted so that the simulated annual cycle remains close to that observed. The flux adjustments have an annual cycle, and do not otherwise vary during the integration. A comprehensive description of the coupled model and flux adjustments is given in Gordon and O'Farrell (1997). The coupled model was integrated for 1000 yr (Hirst et al. 2000), from which the first 100 yr were discarded, leaving 900 yr to analyze. This long data record provides an opportunity to resolve decadal timescales. Unless otherwise noted, the model data used in this study are annually averaged.

3. Spatial and temporal characteristics of modeled Pacific variability

Spatial and temporal characteristics of the simulated Pacific variability are examined using empirical orthogonal function (EOF) analysis of annually averaged upper ocean (0–270-m integrated) heat content over the Pacific basin, from 60°S–60°N to 110°E–60°W. For reference, this region is boxed in Fig. 1. The data at each spatial point are detrended and, for some of the analysis, filtered. EOF analysis is performed on the area-weighted covariance matrix. The principal components (PCs) obtained from the analysis are used to describe the temporal characteristics of Pacific variability. Spatial patterns are obtained by regressing various (detrended) data

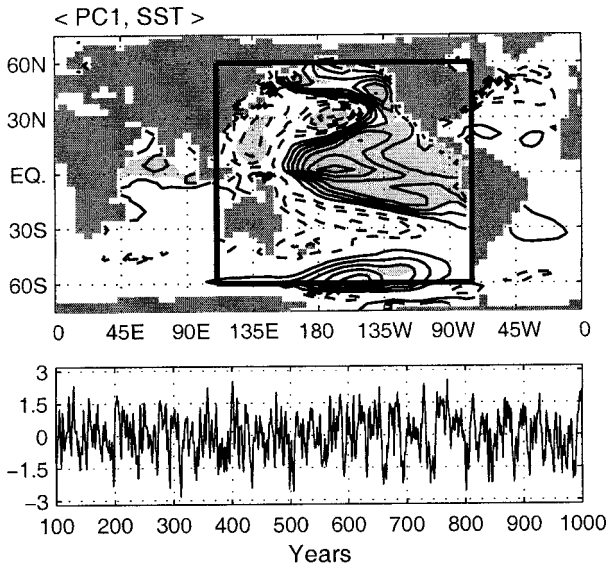

FIG. 1. Spatial and temporal structure of modeled Pacific variability. (top) Global SST regressed onto PC1 of Pacific HC270; contour interval 0.05 K (std dev)$^{-1}$. Negative contours are dashed, the zero contour is omitted. Light shading indicates regions where PC1 explains >25% of the detrended SST variance. The box indicates the region over which the EOF/PC analysis was performed. (bottom) The standardized PC1 of Pacific HC270. Units are in std dev. No smoothing has been applied to the annual data.

onto the standardized PCs, and hence have units ''per standard deviation.''

a. Unfiltered Pacific variability

The leading ''mode'' resulting from the above EOF analysis of unfiltered 0–270-m heat content (HC270) is used to describe Pacific variability. This leading mode explains 23% of the variance of HC270 over the Pacific basin, and is well separated from the remaining EOFs, each of which explains less than 15% of the total variance. The first PC time series (PC1) as well as the regression map of SST onto PC1 are plotted in Fig. 1. Visual inspection of PC1 shows variability on all timescales, from interannual to centennial, though decadal timescales stand out. Further analysis of bandpass-filtered SST confirms that the dominant spatial features in Fig. 1 are found on timescales ranging from interannual to centennial. Similarly, the same mode (statistically) is found in each half of the data, confirming the robustness of the leading mode.

The regression map of SST onto PC1 (Fig. 1) bears a strong resemblance to the global pattern found by Walland et al. (2000) in the same model, and to observed ENSO-related SST anomalies (Zhang et al. 1997; Wallace et al. 1998). In the Pacific, SST anomalies are dominated by an equatorially symmetric pattern of warm anomalies in the Tropics and high latitudes, and cold anomalies in midlatitudes. The equatorial anomalies are centered just east of the date line, with a maximum amplitude of about 0.35°C. [The standard deviation of the monthly modeled cold tongue (CT) index[2] (σ = 0.31°C) is just under half the standard deviation of the observed CT index (σ = 0.71°C), where the latter is based on annually averaged data from the Comprehensive Ocean–Atmosphere Data Set (Fletcher et al. 1983) from 1900 to 1995.] Like many other global coupled models, the maximum warming simulated by the CSIRO CGCM is centered in the central Pacific, instead of along the eastern edge of the basin, as observed. Due to too coarse vertical resolution, the model's thermocline is much more diffuse than observed. Hence, the effect of upwelling in the eastern equatorial Pacific is likely subdued. In general, the broad meridional extent of the simulated Pacific equatorial SST anomalies is more akin to that of the interdecadal ENSO-like SST anomalies than to those relating to ENSO (cf. Fig. 1 with Figs. 11 and 12 of Zhang et al. 1997). In the Northern Hemisphere, the mid- and high-latitude SST anomalies are centered equatorward of their observed counterparts, while the SST anomalies in the Southern Hemisphere bear a much closer resemblance to observations (cf. Garreaud and Battisti 1999). Warm anomalies in the northern Indian Ocean, and two bands of positive SST anomalies along 20°N and 30°S in the Atlantic Ocean are consistent with ENSO-related SST anomalies found in Wallace et al. (1998), and in REOF1 of Kawamura (1994).

The shading in Fig. 1 indicates regions where PC1 explains more than 25% of the unfiltered SST variance, and shows that the SST variability explained by PC1 is dominated by changes in the Tropics. In fact, PC1 is highly correlated with the leading PC from EOF/PC analysis of tropical HC270 (30°S–30°N, 110°E–75°W) ($r = -0.97$),[3] as well as other measures of tropical variability, such as the CT index ($r = 0.89$), and the modified Southern Oscillation index (SOI*) as used by Zhang et al. (1997) ($r = -0.79$).[4] The high correlation between PC1 and the leading PC of tropical HC270 indicates that either index describes the same phenomenon, and that PC1 is dominated by equatorial variability. Furthermore, the CT index and the SOI* are highly anticorrelated ($r = -0.89$; Zhang et al. 1997, find a correlation of $r = -0.81$ between the observed CT index and the SOI*), suggesting that coupling is important to the modeled tropical variability. The small amplitude of equatorial SST anomalies, the resemblance of the SST map in Fig. 1 to ENSO-like decadal variability (Zhang et al. 1997), and the visually decadal nature of PC1 (Fig. 1, lower panel), suggest that in the

[2] The CT index is defined as SST averaged over the region 6°S–6°N, 180°–90°W.

[3] The leading PC of tropical HC270 explains 44% of the tropical HC270 variance.

[4] SOI* is defined in Zhang et al. (1997) as the difference in tropical (20°S–20°N) SLP between the Pacific Ocean from the date line eastward, and the remaining tropical oceans.

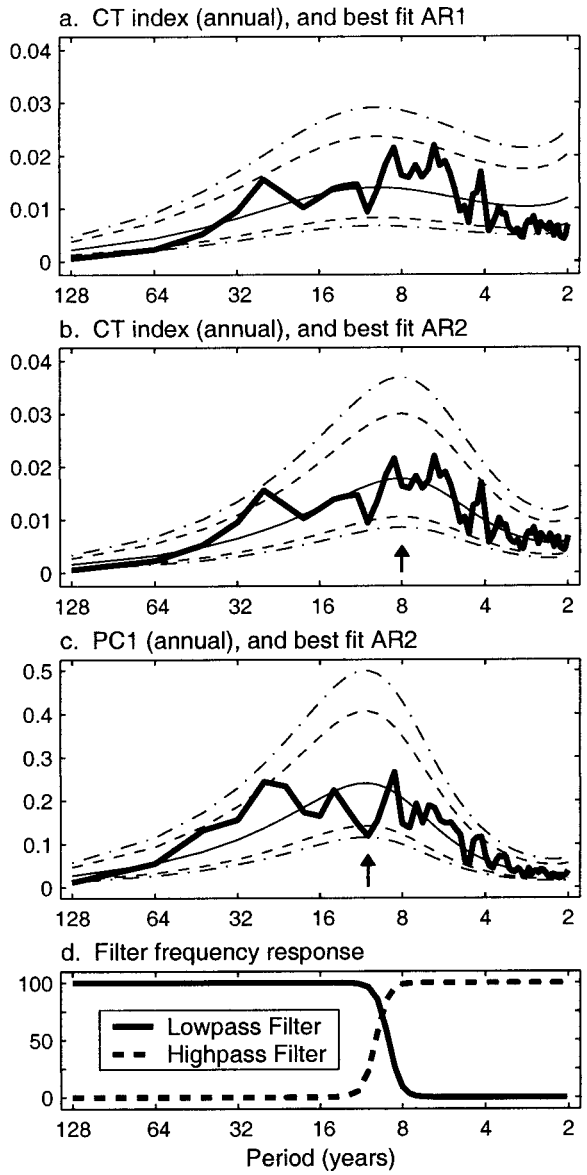

FIG. 2. Power spectra (a)–(c) and filter response functions (d). (a) Annual CT power spectrum (dark solid line), shown together with the best-fit first-order AR (AR1) null hypothesis (thin solid line), and the 95% and 99% confidence levels (thin dashed and dot–dashed lines, respectively). (b) As in (a), except the best-fit second-order AR (AR2) null hypothesis and respective confidence limits are shown. (c) As in (b), except based on PC1 (see text). For (a)–(c), the product of frequency and variance is plotted against the natural log of frequency. The arrows in (b) and (c) indicate the periodic timescales inferred by the theoretical AR2 spectra. In (d), the frequency response function for the 10-yr high-pass (dashed) and 9-yr low-pass (solid) filters are plotted in units of percent variance retained.

interannual band, modeled variability is subdued compared to observations.

To investigate the temporal structure of variability in the model, spectral analysis is performed on the modeled annual CT index, as well as on PC1. The spectrum of the annual CT index is shown due to the high correlation between PC1 and the annual CT index. It is noted that due to this high correlation, the two spectra are not independent realizations. However, the same general features emerge in each half of the data when each time series is split in half. Similarly, a separate CT index from an independent coupled simulation at CSIRO (of 10 000-yr duration) using the same coupled model reproduces the temporal structure of the CT index used in this study, confirming the conclusions in this section.

The power spectra of the simulated annual CT index and PC1 of the upper-ocean heat content are shown in Fig. 2 along with the respective autoregressive (AR) null hypotheses and the 95% and 99% confidence ratios on these null hypotheses. Note that in Fig. 2, the product of frequency and power is plotted against the natural log of frequency, so that the area under the curve in a particular frequency band is equal to the variance contained within that band. For reference, the same power is contained in periods longer than 10 yr as is contained in the 2–9-yr interannual band, confirming the visual impression (Fig. 1) that modeled decadal variability is as energetic as the modeled interannual variability. Furthermore, this plotting convention produces a local maximum at 2π times the inferred damping timescale of a theoretical AR1 spectrum, and at the inferred periodic timescale of a theoretical AR2 spectrum. The periodic timescale inferred by the theoretical AR2 null hypotheses is indicated by the arrows in Figs. 2b and 2c.

The choice of an appropriate AR null hypothesis is motivated by several factors. First, the partial autocorrelation function for the annual CT index is examined. For an AR(n) process, the partial autocorrelation function will be indistinguishable from zero for lags τ greater than n (von Storch and Zwiers 1999). The partial autocorrelation function of the annual CT index is indistinguishable from zero for lags greater than 2, indicating that an AR2 process should ''best fit'' the CT spectrum. Objective tests for AR order (see von Storch and Zwiers 1999) confirm that an AR2 process best fits the data. For comparison with previous studies (Cai and Whetton 2001; Walland et al. 2000) and with the AR2 null hypothesis, we show the AR1 null hypothesis in Fig. 2a. The AR1 null hypothesis clearly overestimates power at periods shorter than about 4 yr, and longer than 64 yr. This overestimate is significant at the 95% and 99% level for numerous spectral estimates. Furthermore, the AR1 process underestimates power for 6–10-yr periods. Thus, we reject the AR1 null hypothesis, and compare the spectra to an AR2 null hypothesis.

The most striking feature of each spectrum is the agreement with the theoretical AR2 process. Starting with the annual CT index, the best-fit AR2 spectrum produces a periodic timescale of 8 yr. Walland et al. (2000) and Cai and Whetton (2001) find spectral peaks at about 8 yr in both the first PC of global SST and the Niño-3 index,[5] that are significantly distinguishable

[5] The Niño-3 index is formed by averaging SST over the region (5°S–5°N, 90°–150°W).

from the AR1 null hypothesis with which they compare the spectra. The 8-yr timescale should not be interpreted as a strict periodicity in the Tropics, but rather the center of a range of preferred periodic timescales. This interpretation is supported by investigating various 128-yr segments in which the peak of the best-fit AR2 process ranges from 6 to 10 yr. Other interesting features of the semiannual CT spectrum include a peak at about 4 yr that is not significant, and a 25-yr peak that is significant at the 95% confidence level. The 25-yr peak is reproduced in both halves of the data, as well as the CT index from the independent CSIRO CGCM simulation, and is discussed by Walland et al. (2000) and Cai and Whetton (2001). The 4-yr spectral peak is variable throughout the model integration. The power spectrum of PC1 of annually averaged upper-ocean heat content (Fig. 2c) is very similar to that of the semiannual CT index, as should be expected by the large correlation between PC1 and the annual CT index.

b. Interannual and decadal variability

To distinguish between interannual and decadal variability in the model, we construct high-pass and low-pass filters, and apply each to the model data. Two 9-point Butterworth filters are used: a high-pass filter with a 10-yr cutoff, and a low-pass filter with a 9-yr cutoff. Each filter's frequency response is shown in Fig. 2d. Though there is a slight overlap between the two filters, the shared variance is small. Results are generally insensitive to the exact cutoff frequency of the high-pass or low-pass filter. For example, the structure, evolution, and mechanism governing 10-yr high-pass-filtered variability are nearly identical to those governing 12 yr, or 7-yr high-pass-filtered variability, or 4–12-yr bandpass-filtered variability. The same is generally true of the low-pass filter. Thus, our choice of a specific filter cutoff is somewhat arbitrary. A brief note on the 25-yr spectral peak will be presented in section 5c.

The first PC resulting from EOF analysis of the 10-yr high-pass-filtered and 9-yr low-pass-filtered HC270 are used to represent interannual and decadal variability in the model. These first PCs of high-pass-filtered and low-pass-filtered HC270 (hereafter referred to as HPC1 and LPC1, respectively) explain 24% and 27% of the high-pass- and low-pass-filtered HC270 variance in the Pacific, respectively, and are well separated from higher modes. For reference, HPC1 and LPC1 explain 9% and 17%, respectively, of the unfiltered HC270 variance in the Pacific. It is noted that EOF analysis of filtered data need not produce the same results as filtering the results from EOF analysis of unfiltered data. However, the correlation between HPC1 or LPC1 and the high-pass-filtered or low-pass-filtered PC1 (obtained from unfiltered data) is $r = 0.92$ and $r = 0.98$, respectively; thus, essentially the same variability is being captured. Whether the physics responsible for this variability is the same for both timescales still needs to be determined.

Spatial regression maps of SST, SLP, wind stress (τ), and precipitation onto HPC1 and LPC1 are shown in Fig. 3. Differences in the Tropics between the interannual and decadal maps are subtle, and agree well with observations (Zhang et al. 1997; Garreaud and Battisti 1999; Knutson and Manabe 1998; Yukimoto et al. 1996). Though both SST regression maps are dominated by a warm tropical Pacific, tropical SST anomalies in the decadal map are meridionally broader than those in the interannual map, especially in the eastern and central Pacific. For both timescales, the dominant feature in the equatorial SLP map (center panel) is the familiar east–west seesaw of surface pressure between the eastern Pacific, and the Indian Ocean (the Southern Oscillation). Westerly wind stress anomalies near the equator are collocated with the westward SLP gradient (and eastward SST gradient) in both maps. However, there are subtle, but important, differences in the wind stress curl (not shown) just north of the equator on interannual and decadal timescales. West of the date line, the wind stress curl for both timescales is positive, but is larger, and centered closer to the equator for interannual timescales. East of the date line, the wind stress curl is weak for interannual timescales, and is negative for decadal timescales (see Vimont 2000, for a more complete analysis of the simulated wind stress curl). Subtle differences in the structure of wind stress curl near the equator cause large differences in the Rossby signals that are generated (see section 5). Thus, these differences are important. For both timescales, precipitation anomalies (shading beneath wind stress vectors) include an eastward shift in equatorial precipitation, and an intensification and southeastward extension of the South Pacific convergence zone (SPCZ). Consistent with results from Garreaud and Battisti (1999), the intensification and southeastward extension of the SPCZ is more pronounced on decadal timescales. The high-pass-filtered heat content is not related to precipitation anomalies in the eastern Pacific ITCZ, in contrast to observed ENSO-related precipitation anomalies that show a southward displacement of the ITCZ in the eastern Pacific associated with anomalously warm equatorial SST (and presumably increased heat content).

Similar to the Tropics, the mid- and high-latitude anomalies associated with HPC1 and LPC1 share many of the same qualitative characteristics, though differences exist. Though negative midlatitude SST anomalies are evident on both timescales, in the interannual band the amplitude of the negative midlatitude SST anomalies are half that of the positive equatorial SST anomalies, while on decadal timescales the amplitude of the tropical and midlatitude SST anomalies are nearly equal. Mid- and high-latitude decadal SST anomalies are located slightly poleward of their interannual counterparts, and have larger amplitude, especially along the ocean's western boundary—presumably a reflection of differing roles of ocean dynamics on the two timescales in the high latitudes (e.g., Frankignoul et al. 1997; Xie et al.

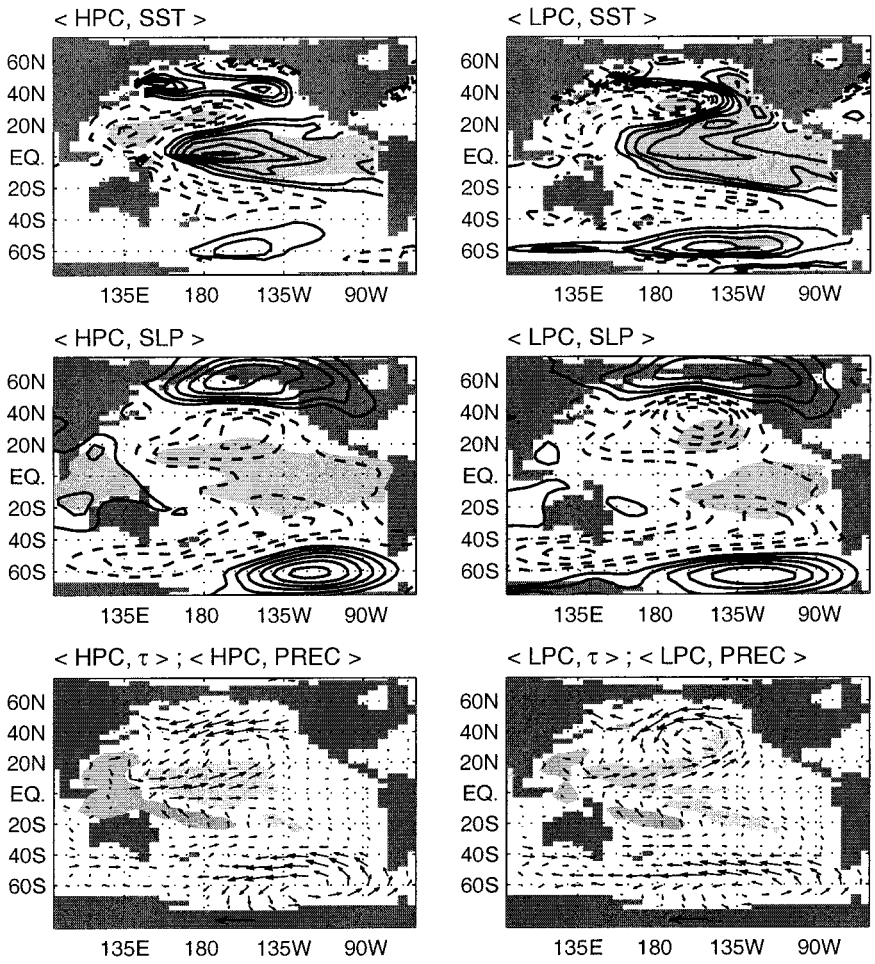

FIG. 3. Regression maps of various fields onto HPC1 (left column, interannual), and LPC1 (right column, decadal). (top row) SST; contour interval 0.05°C (std dev)$^{-1}$. Light shading denotes regions where HPC1 or LPC1 explains more than 20% of the *unfiltered* SST variance. (middle row) SLP; contour interval 0.1 hPa (std dev)$^{-1}$. Light shading denotes regions where HPC1 or LPC1 explains more than 20% of the *unfiltered* SLP variance. (bottom row) Wind stress (τ) and precipitation; reference arrow in the center of the shaded area at the bottom denotes a wind stress of 0.1 dyn cm^{-2} (std dev)$^{-1}$. Light or dark shading denotes regions where precipitation anomalies exceed 0.15 or -0.15 mm day^{-1} (std dev)$^{-1}$ respectively. Negative contours are dashed, the zero contour is omitted.

2000; Schneider et al. 2002). An equatorially symmetric pattern of low SLP in midlatitudes, and high SLP in high latitudes is evident in both interannual and decadal timescales. Unlike observations, this pattern more closely resembles the North Pacific Oscillation of Walker and Bliss (1932) than a deepened Aleutian low. Like the SST map, decadal SLP anomalies are centered poleward of, and are stronger than their interannual counterparts. It should be noted that the pattern of Northern Hemisphere SLP anomalies associated with LPC1 bears a stronger resemblance to the first EOF of modeled SLP (not shown) over the North Pacific than that associated with HPC1. An examination of the upper-ocean heat budget in the midlatitudes and the surface momentum and heat flux anomalies indicate that the midlatitude SST anomalies are atmospherically driven (Vimont 2000).

4. Tropical interannual variability

In this section we will document the mechanisms responsible for the interannual variability in the model. This will establish a reference against which the physics of the simulated decadal variability can be compared. Additionally, if the mechanisms governing interannual variability in the model resemble those found in other modeling and observational studies (Battisti 1988; Battisti and Hirst, 1989; Mantua and Battisti 1994; Neelin et al. 1998; Schopf and Suarez 1988; Suarez and Schopf 1988), we can increase our confidence that the model

is also reproducing the correct mechanism for decadal variability. Readers not interested in a detailed description of the equatorial heat budget can skip to section 4b, which contains a distillation of the essential results.

To investigate the evolution and physical mechanisms associated with the model's tropical variability, the upper 270 m of the ocean are split into the top 80 m (*upper level*), and the layer from 80 to 270 m (*lower level*). As the model mixed layer extends to at least 50-m depth, changes in the upper level strongly reflect changes in mixed layer properties. Similarly, because the maximum vertical temperature gradient in the equatorial region is typically found below 80 m, changes in the lower-level heat content signify changes in the depth of the model's thermocline; a deepened (shoaled) thermocline implies increased (decreased) lower-level heat content. Thus, the separation of the upper 270 m generally distinguishes between mixed layer processes (upper level) and processes involving changes in the depth of the equatorial thermocline (lower level).

The evolution of ocean heat content (HC) anomalies in the equatorial region is described through the lagged regression maps of the annually resolved upper- and lower-level HC onto HPC1, in the left and right columns of Fig. 4, respectively. The upper-level equatorial HC anomalies undergo a standing oscillation, though slight north–south asymmetries exist. These asymmetries are explored in a companion study (VBH). During the year preceding a warm event (lag -1), the upper-level HC anomalies are mainly found in the Northern Hemisphere. By lag 0, the surface warms in a pattern that closely resembles the regression map of SST onto HPC1 in Fig. 3. The surface HC anomalies have significantly decayed by lag $+1$ yr.

In contrast to the upper level, the lower-level HC anomalies undergo a well-defined evolution. The standing oscillation at the surface with eastward propagation at depth is consistent with observed SST and thermocline depth anomalies associated with ENSO (Wallace et al. 1998). During the development of a warm event (lag -1 yr), the equatorial thermocline has deepened across the entire Pacific. By lag 0, this deepening has progressed to the eastern equatorial Pacific, while in the western subtropical and tropical Pacific (3°–20°N, 120°–180°E), large negative HC anomalies indicate a shoaled thermocline. This shoaling appears to progress equatorward and eastward by lag $+1$, eroding the deepened thermocline in the central and eastern Pacific. The evolution of upper- and lower-level heat content anomalies are consistent with the delayed oscillator theory of ENSO. A similar evolution of tropical subsurface temperature anomalies in the present simulation is presented by Cai and Whetton (2001).

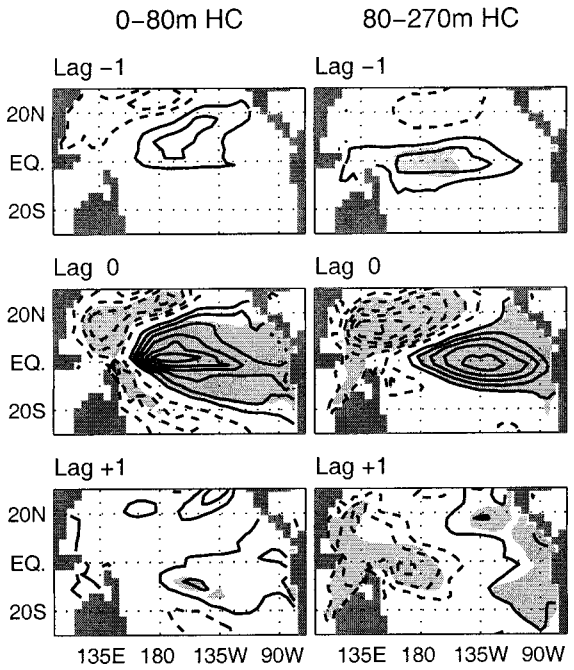

FIG. 4. Lagged regression of annually averaged upper-level (0–80 m, left column) and lower-level (80–270 m, right column) heat content onto HPC1. Shown are lag -1 yr (top row), lag 0 (middle row), and lag $+1$ yr (bottom row). Contour interval 15×10^6 J m^{-2} (std dev)$^{-1}$ (left), 30×10^6 J m^{-2} (std dev)$^{-1}$ (right). Negative contours are dashed, the zero contour is omitted. Light shading denotes regions where HPC1 explains more than 20% of the 10-yr high-pass-filtered variance of the respective field.

a. Key processes in the evolution of the interannual ENSO variability

To isolate the physical processes responsible for changes in heat content in the upper and lower level, the individual terms in the heat content tendency equation are examined. This equation is derived by linearizing the temperature tendency equation around a time mean, multiplying by density and the specific heat of water (both assumed constant), and vertically integrating over a layer spanning from depths H_1 to H_2:

$$\underbrace{\rho c_o \frac{\partial}{\partial t}\left(\int_{H_1}^{H_2} T'\, dz\right)}_{(i)} = \underbrace{-\rho c_o \int_{H_1}^{H_2} \left(\overline{u}T'_x + \overline{v}T'_y + \overline{w}T'_z\right)}_{(ii)} \underbrace{+ u'\overline{T}_x + v'\overline{T}_y + w'\overline{T}_z}_{(iii)} dz \underbrace{- HFLX^{\uparrow\prime}|_{z=H_1}^{z=H_2}}_{(iv)} + \underbrace{R'}_{(v)}. \quad (1)$$

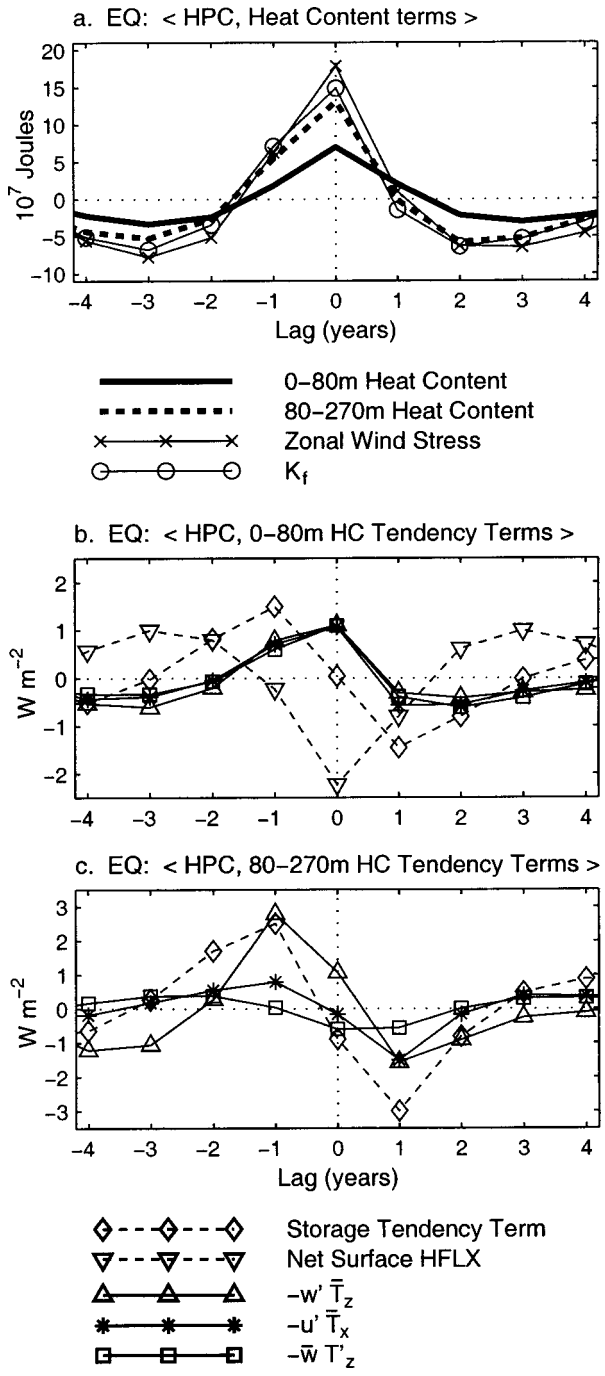

FIG. 5. Lagged regression of annually averaged equatorial (3°S–3°N, 180°–90°W) terms onto HPC1: (a) upper- and lower-level heat content (10^7 J), zonal wind stress averaged over (6°S–6°N, 150°E–150°W) (arbitrarily scaled), and K_f (units arbitrary); (b) upper-level heat content tendency terms (W m^{-2}); (c) lower-level heat content tendency terms (W m^{-2}). Terms in (a) are listed below (a); terms in (b) and (c) are listed below (c).

In Eq. (1), overbars ($\bar{\cdot}$) indicate time mean anomalies; primes $(\cdot)'$ indicate anomalies from the time mean; and subscripts *x, y,* or *z* indicate a zonal, meridional, or vertical partial derivative, respectively. Equation (1) equates the heat storage tendency within a layer (*i*), to the integrated effect of advection by the mean currents acting on anomalous temperature gradients (*ii*), advection by the anomalous currents acting on the mean temperature gradients (*iii*), the convergence of heat flux (*iv*), and a residual term (*v*). The effect of anomalous currents acting on anomalous temperature gradients is assumed small, and subsumed into the residual term. The residual term also includes convection, diffusion, and numerical error associated with calculating discrete derivatives in time and space (see Vimont 2000, for details).

Mechanisms affecting the equatorial heat budget are inferred by examining the contribution of each of the terms in Eq. (1) in the equatorial region. Each term in Eq. (1) is regressed onto HPC1, and the resulting map of regression coefficients is averaged over the region 3°S–3°N, 180°–90°W. The resulting value indicates each term's heating rate [W m^{-2} (std dev)$^{-1}$] for a given lag. Only the terms that significantly contribute to the equatorial heat budget are plotted in Figs. 5b and 5c. These terms are the tendency, net surface heat flux, $-w'\overline{T}_z$, $-u'\overline{T}_x$, and $-\overline{w}T'_z$ terms. Also plotted in Fig. 5a are the lagged regression coefficients of heat content averaged over the same region; wind stress averaged over the region 6°S–6°N, 150°E–150°W; and K_f, the Kelvin wave forcing term,[6] averaged from 120°E to 135°W. The zonal wind stress, and K_f indices are arbitrarily scaled to fit within the figure limits. Figure 5a indicates that the upper-level heat content reaches a maximum at lag 0, indicating the peak of an event. It is noted that the upper-level heat content and zonal wind stress are in phase, reiterating the important role of coupling in producing tropical interannual variability. The maximum development and decay of an event (inferred from the storage tendency term's maximum and minimum, Fig. 5b) occur at lag -1 yr, and lag $+1$ yr, respectively. For reference, the spatial maps of each of the dominant terms in the interannual equatorial heat budget are shown during the development of an event in Fig. 6.

Figure 5b shows that the surface heat flux strongly damps equatorial heat content anomalies throughout the entire event. This requires that equatorial variability be dynamically driven, in contrast to the results of Kitoh et al. (1999). The spatial map in Fig. 6 shows that this damping is closely confined to the equator during the development of an event. Just off the equator, the surface

[6] The Kelvin wave forcing term K_f is generated by projecting the zonal wind stress regression map at a given lag onto the meridional Kelvin wave structure (see Battisti 1988, appendix, for details): $K_f(x, n) = \int_{-\infty}^{\infty} \tilde{\tau}_x(x, y, n)\psi_0\, dy$, where ψ_0 is the meridional Kelvin wave structure, and $\tilde{\tau}_x(x, y, n)$ is the nondimensional zonal wind stress map at lag *n.* Results are generally insensitive to realistic values for the equivalent depth of the first baroclinic mode, used to calculate ψ_0.

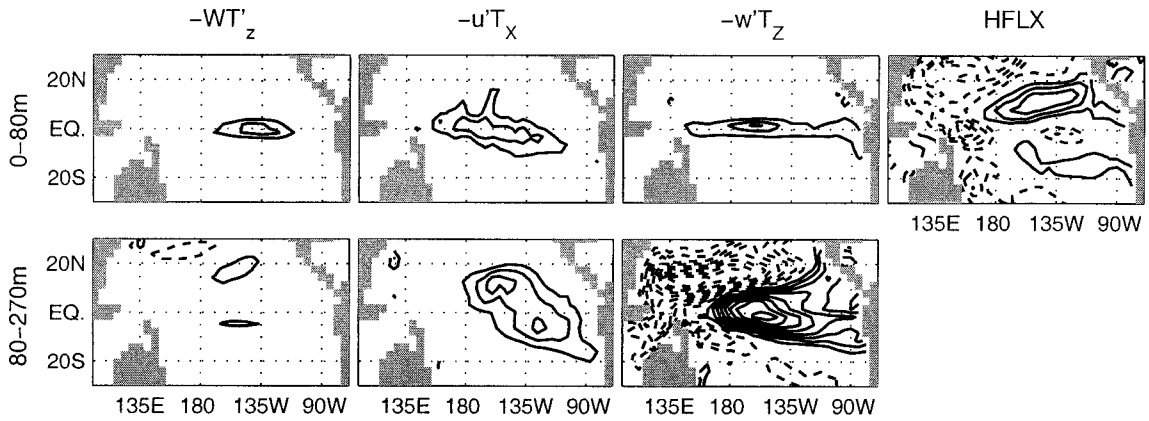

FIG. 6. Lag −1 yr regression maps of upper-level (0–80 m, top) and lower-level (80–270 m, bottom) heat content tendency terms [from Eq. (1)] onto HPC1. From left to right: $-\overline{w}T'_z$, $-u'\overline{T}_x$, $-w'\overline{T}_z$, net surface heat flux. Units: 0.5 W m^{-2} (std dev)$^{-1}$. Negative contours are dashed, the zero contour is omitted.

heat flux acts to spread the upper-level heat content anomalies poleward in the eastern and central Pacific. Inspection of the individual surface heat flux components (Vimont 2000) shows that the net surface heat flux is largely determined by anomalies in shortwave radiative fluxes and latent heat fluxes. These results are consistent with observed eastern Pacific surface heat fluxes associated with ENSO events (Deser 1989). By lag 0, the off-equatorial heating by the surface heat flux weakens, while the surface flux damping along the equator strengthens. During the decay of an event, the net surface heat flux acts to damp the upper-level heat content anomalies across the entire basin.

The dominant dynamic terms in the upper-level heat budget tendency equation ($-w'\overline{T}_z$, $-u'\overline{T}_x$, and $-\overline{w}T'_z$, Fig. 5b) are all in phase, and have nearly equal amplitudes. The first two dynamic terms, $-w'\overline{T}_z$ and $-u'\overline{T}_x$, are easily explained as a local coupled feedback between the zonal wind stress and SST: part of the so-called Bjerkness feedback. Positive SST anomalies (with spatial structure nearly identical to the upper-level HC anomalies in Fig. 4) in the central and eastern equatorial Pacific cause a westerly wind stress anomaly, which drives an anomalous eastward equatorial current, and reduces the climatological Ekman upwelling. Both of these effects tend to warm the surface, due to a climatological westward and upward ocean temperature gradient along the equator. The spatial map of both the $-w'\overline{T}_z$ and $-u'\overline{T}_x$ terms in Fig. 6 show that the maximum warming by both of these terms is tightly confined to the equator, and spread over the longitudinal extent of the wind stress anomalies in Fig. 3. Consistent with increasing westerly zonal wind stress anomalies (Fig. 5), both terms amplify during lag 0, with little change in spatial structure (not shown). By lag +1 the $-u'\overline{T}_x$ term has reversed polarity with similar spatial structure, signifying either the onset of the following cold event, or a strengthening of the trades. The $-w'\overline{T}_z$ term also reverses polarity by lag +1, and has a spatial structure that is confined to the far eastern Pacific. More detailed analysis shows that cooling by the $-w'\overline{T}_z$ term in lag +1 is dominated by anomalous upwelling near 80 m—the climatological depth of the eastern Pacific thermocline. The upper-level $-\overline{w}T'_z$ term relates to changes in the depth of the thermocline, and will be discussed next with the lower-level heat budget.

In the lower level, the evolution of heat content along the equator (dark dashed line in Fig. 5a) is slightly different than at the surface. While the temporal resolution of the model output available to us (annual means) is too coarse to draw robust quantitative conclusions about timing, heat content anomalies in the lower level do appear to slightly lead heat content anomalies at the surface, especially during the decay of the event. A more pronounced lead is seen for the $-w'\overline{T}_z$ and $-u'\overline{T}_x$ terms in Figs. 5b and 5c, where changes in the lower-level lead changes in the upper level by 1 yr. We will discuss this lead shortly.

The dominant heating terms in Eq. (1) for the lower level (cf. Fig. 5c) is the $-w'\overline{T}_z$ term, with a lesser contribution from the $-u'\overline{T}_x$ and $-\overline{w}T'_z$ terms. The first two dynamic terms, $-w'\overline{T}_z$ and $-u'\overline{T}_x$, relate to anomalous currents associated with coupled equatorial signals. A westerly wind stress anomaly in the central Pacific will locally produce an eastward-propagating, downwelling signal. The associated eastward and downward anomalous velocities act on a climatological westward and upward temperature gradient, warming the eastern and central equatorial Pacific. This effect is clearly seen in Fig. 6, and likely explains the lower-level eastward-developing positive heat content anomalies between lag −1 and lag 0 in Fig. 4. Figure 5c shows that at lag 0, warming by the $-w'\overline{T}_z$ and $-u'\overline{T}_x$ terms wanes (though westerly wind stress anomalies and K_f both continue to amplify), while they are largely responsible for the decay of an event in lag +1.

In both the upper and lower levels (Figs. 5b and 5c), the $-\overline{w}T'_z$ term is explained by coupled equatorial

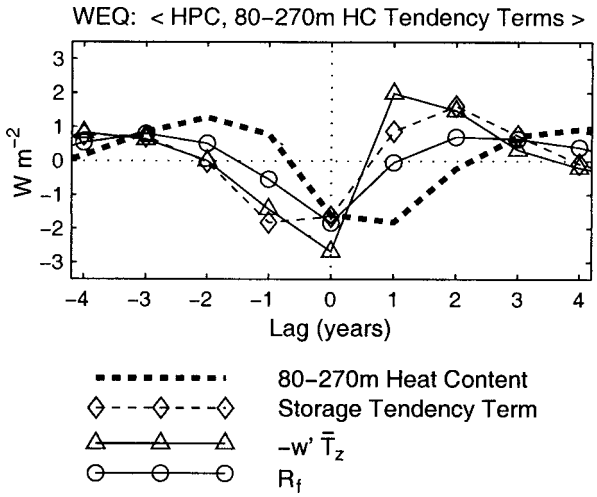

FIG. 7. Lagged regression of annually averaged western equatorial Pacific (10°S–10°N, 120°–165°E) lower-level heat content (scaled), and heat content tendency terms (W m^{-2}) onto LPC1. Also shown is the Rossby wave forcing term, R_f (see text).

waves, and is due to a displacement of the climatological thermocline. As a downwelling signal propagates eastward, the thermocline deepens, reducing the climatological vertical temperature gradient in the upper level and increasing it in the lower level, and thus contributing to warming in the upper level, while partially compensating the warming by $-w'\overline{T}_z$ in the lower level. Though the lower-level cooling is not clearly seen at lag -1 in Fig. 6, it does appear by lag 0 (not shown). Note that while the $-\overline{w}T'_z$ term acts to cool the lower level, the strongest mean upwelling is in the upper level. Hence, a deepening of the thermocline implies a net heat content increase by the $-\overline{w}T'_z$ term over the top 270 m. As the $-\overline{w}T'_z$ term warms the upper level, increased SST in the eastern Pacific will drive a stronger westerly wind stress anomaly, completing a coupled positive feedback in the central and eastern Pacific. In lag $+1$ the $-\overline{w}T'_z$ term starts to cool the upper level in the central Pacific. This is consistent with the negative lower-level heat content anomalies in Fig. 4, and a shoaling of the thermocline in the central Pacific.

The equatorial zonal wind stress and K_f both amplify from lag -1 to lag 0 (Fig. 5a), which, by the arguments above, would imply increased equatorial warming in the lower level by the $-w'\overline{T}_z$ and $-u'\overline{T}_x$ terms. However, the lower-level $-w'\overline{T}_z$ and $-u'\overline{T}_x$ terms (Fig. 5c) peak at lag -1, one year *prior* to the K_f and zonal wind stress. Together, the large negative lower-level heat content anomalies in the western tropical Pacific (around 10°S–10°N, 120°–165°E), the wind stress anomalies, K_f, and the 1-yr lead between the lower and upper levels suggest an important role of nonlocal forcing, such as western boundary reflections. To investigate this possibility, the lagged regression coefficient of the dominant heat budget terms, as well as the (scaled) heat content for the western tropical Pacific are shown in Fig. 7 (all terms are averaged over 10°S–10°N, 120°–165°E). Also plotted is the Rossby wave forcing term[7] (R_f) averaged from 120°E to 135°W. Note that R_f is scaled by the same amount as K_f, so their relative amplitudes may be compared.

In the western tropical Pacific, the heat budget (Fig. 7) is dominated by a balance between the storage tendency term and the $-w'\overline{T}_z$ term. The cooling at lag -1 and lag 0 by the $-w'\overline{T}_z$ term occurs simultaneously with an implied cooling by locally forced Rossby waves (from R_f). Thus, the anomalous upwelling in the western equatorial Pacific represents Rossby wave activity that is forced by the same wind stress anomalies that are producing the K_f term (Fig. 5a). Provided the westward-propagating Rossby signals reflect off the western boundary and propagate eastward along the equator, they will compete with the locally forced downwelling signal in the central equatorial Pacific. This competition can be seen in Fig. 5 as warming by the lower-level equatorial $-w'\overline{T}_z$ and $-u'\overline{T}_x$ terms decreases from lag -1 to lag 0, though westerly zonal wind stress anomalies and K_f both continue to increase (see Fig. 5). Thus, the positive feedback in the central tropical Pacific is countered by a negative feedback involving freely propagating signals from the western tropical Pacific. The operation of this negative feedback on interannual timescales will be further discussed in conjunction with decadal timescales in section 5.

b. Physics of the interannual ENSO variability

Results from the preceding tropical heat budget analysis indicates that the simulated interannual ENSO evolves consistently with the delayed oscillator theory of ENSO, albeit heavily damped due to the overly crude ocean resolution (see Ng and Hsieh 1994). The local positive feedback between wind stress, thermocline depth, and SST (the so-called Bjerkness feedback) causes an amplification of SST anomalies in the central and eastern Pacific. The local Bjerkness feedback is countered by the ocean memory—the same central Pacific wind stress anomalies associated with the Bjerkness feedback force free westward-propagating signals that reflect off the western boundary, and provide a negative feedback in the central Pacific some time later. The preferred period (6–9 yr) inferred by the AR2 fit to the spectrum is longer than that in nature (3–5 yr), likely due to the weaker upwelling in the model, and by slowed wave speeds, both caused by coarse model resolution (see Wakata and Sarchik 1992; Ng and Hsieh 1994).

[7] To generate a cleaner figure, the effect of the first four symmetric Rossby wave forcing terms (generated in a similar fashion as K_f) has been combined into one term, R_f. Each mode has been weighted by its contribution to the amplitude of a Kelvin wave reflected off the western boundary (see Battisti 1988, appendix 2b). Thus, given forcing amplitudes R_2, R_4, R_6, and R_8 for the first four symmetric Rossby waves, the Rossby wave forcing term is defined as $R_f = 0.71\ R_2 + 0.17\ R_4 + 0.10\ R_6 + 0.06\ R_8$.

The long preferred period in the CSIRO model will be further discussed in section 6.

At this point, a note on the coarse temporal resolution is in order. Results presented in this section are based on annually averaged model output. This time step is too coarse to resolve characteristics of freely propagating Kelvin and Rossby waves. However, during ENSO, the ocean does not evolve through propagation of individual Kelvin and/or Rossby waves; instead, the ocean is continuously forced by the atmospheric wind stress associated with the coupled dynamics. Timescales associated with coupled basin adjustment (ENSO) are longer than those associated with individual equatorial waves. Further, it is noted that the standard deviation of the modeled monthly CT index ($\sigma = 0.31$ K) is very close to that of the modeled annual CT index ($\sigma = 0.28$ K). Thus, there is little subbiennial power in the CT index, and annual resolution is likely adequate in describing the basic physics of the modeled interannual variability. Finally, the standard deviation of the model's CT index peaks during boreal summer. Provided that this peak indicates a peak of the model's ENSO variability, the averaging convention (Jan–Dec) fortuitously captures the peak of an event, adding credence to the annually averaged results.

5. Tropical decadal variability

In section 4, it was shown that coupled processes in the Tropics set up a positive feedback along the equator in the eastern half of the basin (the Bjerkness feedback) that will amplify equatorial SST anomalies. Thus, any physical mechanism that induces a change in the zonal SST gradient or in the zonal wind stress along the equator should engage this feedback to produce an amplified, coupled response. Noting the similarity between the structure of interannual and decadal heat content anomalies in Fig. 3, it is likely that coupled equatorial dynamics are responsible for the structure of variability on decadal timescales as well as interannual timescales. However, this needs to be verified. It was also shown in section 4 that upwelling tropical Rossby signals are evident in the western subtropical Pacific on interannual timescales; these signals counter the positive Bjerkness feedback for interannual timescales. For the decadal timescale, it will be important to analyze whether both mechanisms act in the same way. If the western boundary reflection does act to counter the positive feedback on decadal as well as interannual timescales, then some other physical mechanism is required to account for the enhanced (decadal) persistence of a warm event. If the opposite is true, then the positive feedback will simply continue until an event decays away by diffusive or stochastic processes. Readers not interested in a detailed description of the equatorial heat budget can skip to section 5b, which contains a summary of the essential results.

As in section 4, the evolution of equatorial upper- and lower-level decadal HC anomalies are described through lagged regression onto LPC1, as shown in Fig. 8. Characteristics of decadal HC evolution are quite similar to characteristics of interannual HC evolution. Specifically, the left column of Fig. 8 shows that the upper-level HC evolves as a standing oscillation, with a pattern very similar to that seen in the regression map of SST onto LPC1 in Fig. 3. The lower-level HC anomalies evolve much differently than the upper level. Starting at lag -5, positive lower-level equatorial heat content anomalies indicate that the equatorial thermocline is deeper than normal across the entire equatorial Pacific. The equatorial thermocline continues to deepen in

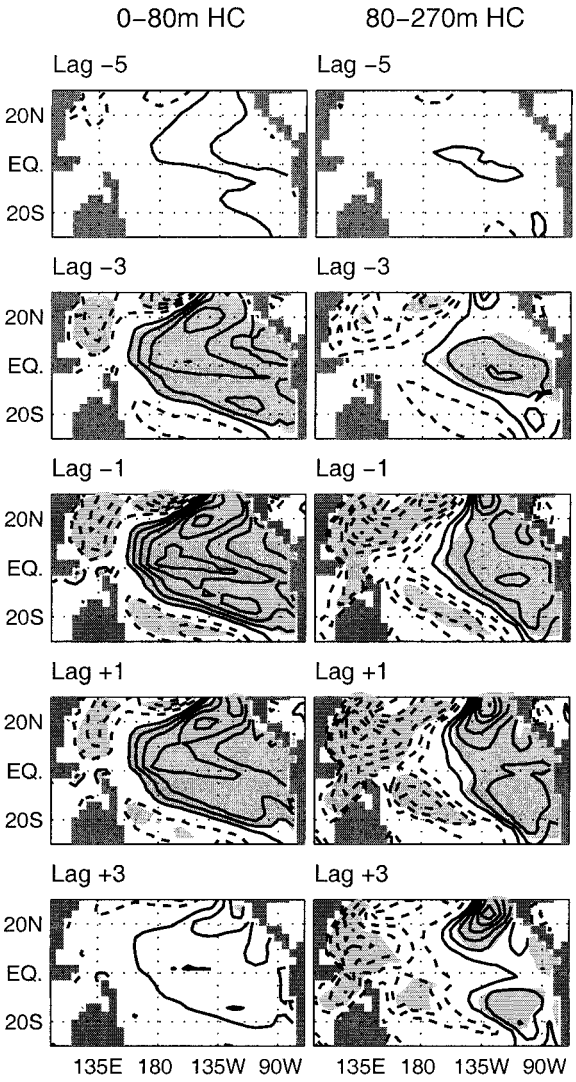

FIG. 8. Lagged regression of annually averaged upper-level (0–80 m, left column) and lower-level (80–270 m, right column) heat content onto LPC1. Shown (from top to bottom) are lags -5, -3, -1, $+1$, and $+3$ yr. Contour interval 15×10^6 J m^{-2} (std dev)$^{-1}$ (left), 30×10^6 J m^{-2} (std dev)$^{-1}$ (right). Negative contours are dashed, the zero contour is omitted. Light shading denotes regions where LPC1 explains more than 20% of the 9-yr low-pass-filtered variance of the respective field.

the eastern and central Pacific from lag −5 to lag −1. At the same time, negative heat content anomalies develop off the equator in the western subtropical Pacific, indicating a shoaling thermocline there. In lag +1, the negative HC anomalies in the western subtropical Pacific begin to dominate the equatorial regions, eroding away the positive HC anomalies in the eastern basin. By lag +3, a tongue of negative HC anomalies along the equator indicates a shoaling thermocline across the basin.

Differences between the evolution of interannual and decadal HC anomalies in Figs. 4 and 8 are subtle, but important. Most notable is the broad meridional structure of equatorial decadal HC anomalies in the eastern Pacific, compared to the structure of interannual HC anomalies. This broadening is especially evident in the lower level. In the western tropical Pacific, negative decadal HC anomalies develop slightly poleward of their interannual counterparts. Provided these negative HC anomalies are due to Rossby signals, the poleward shift strongly affects the energy that is returned eastward (via Kelvin signals) when these Rossby signals reach the western boundary (e.g., Clarke 1983).

a. Key processes in the evolution of the decadal ENSO-like variability

Mechanisms responsible for the evolution of decadal variability are illuminated by a lagged regression analysis of the heat content, zonal wind stress, Kelvin wave forcing term (K_f), and the terms in Eq. (1) that significantly contribute to the heat budget: the storage tendency term, surface heat flux, $-w'\overline{T}_z$, $-u'\overline{T}_x$, and $-\overline{w}T'_z$ terms. Each of these terms is regressed onto the first PC of the low-pass-filtered HC270 (LPC1), averaged over the equatorial region (the same region as in Fig. 5), and plotted in Fig. 9. The equatorial upper- and lower-level heat contents (Fig. 9a) peak just prior to lag 0 and lag −1 yr, respectively. The maximum and minimum of the storage tendency terms occur at lag −4 and lag +3 for the upper level, and at lag −4 and −2 for the lower level (Figs. 9b and 9c). We define the development, peak, and decay of a decadal event at lag −4, lag −1, and lag +2, respectively. To aid interpretation of the individual terms, spatial maps of the $-\overline{w}T'_z$, $-u'\overline{T}_x$, $-w'\overline{T}_z$, and surface heat flux terms are shown during the development of an event in Fig. 10. It is noted that the zonal wind stress and upper-level heat content are in phase in Fig. 9a, indicating an important role of coupling on decadal timescales.

The upper-level decadal heat content tendency (Fig. 9b) is dominated by the same terms [from Eq. (1)] that dominate interannual timescales; the storage tendency term is balanced by the surface heat flux, $-w'\overline{T}_z$, $-u'\overline{T}_x$, and $-\overline{w}T'_z$ terms. As on interannual timescales, the surface heat flux strongly damps the upper-level HC anomalies, requiring that equatorial heat content changes are dynamically driven on decadal timescales. The

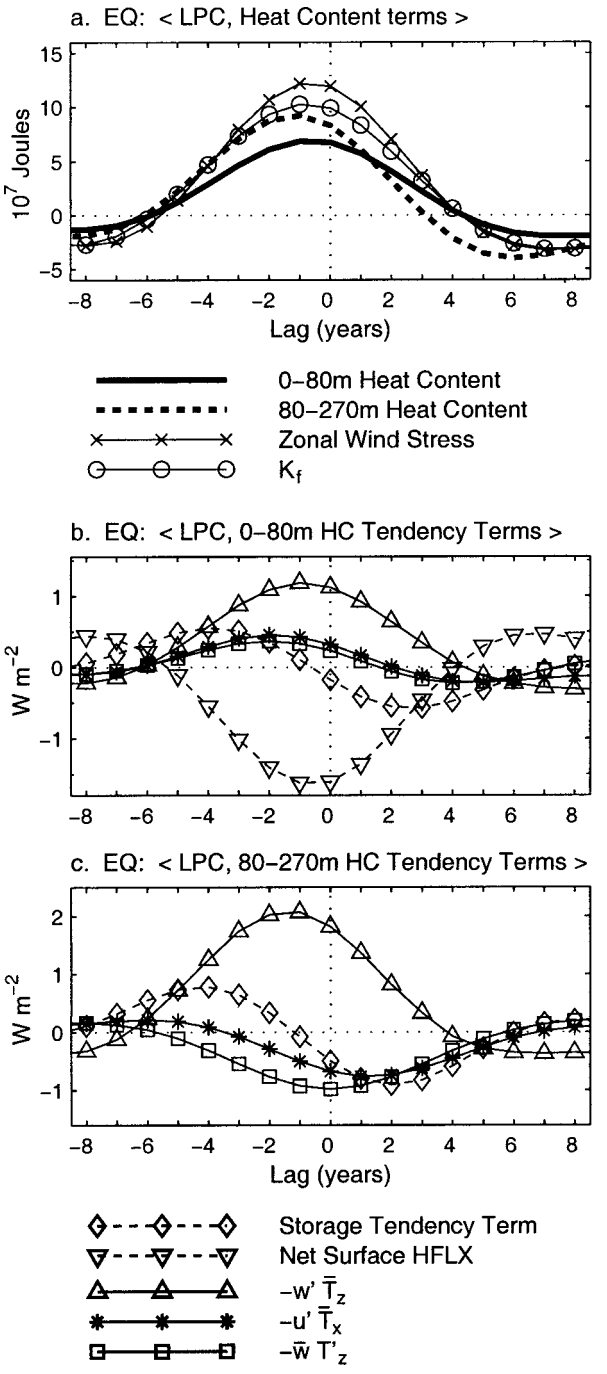

FIG. 9. Lagged regression of annually averaged equatorial (3°S–3°N, 180°–90°W) terms onto LPC1: (a) upper- and lower-level heat content (10^7 J), zonal wind stress averaged over (6°S–6°N, 150°E–150°W) (arbitrarily scaled), and K_f (units arbitrary); (b) upper-level heat content tendency terms (W m^{-2}); (c) lower-level heat content tendency terms (W m^{-2}). Terms in (a) are listed below (a); terms in (b) and (c) are listed below (c).

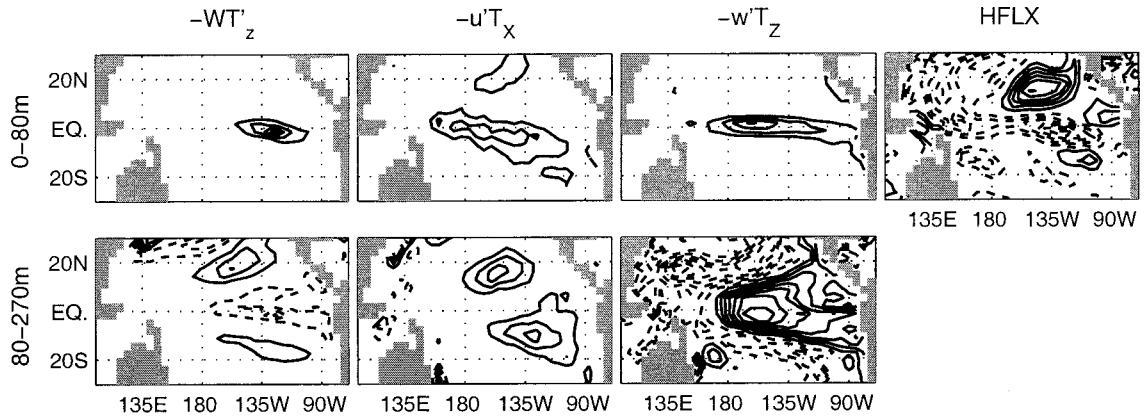

FIG. 10. Lag −4 yr regression of upper-level (0–80 m, top) and lower-level (80–270 m, bottom) heat content tendency terms [from Eq. (1)] onto LPC1. From left to right: $-\overline{w}T'_z$, $-u'\overline{T}_x$, $-w'\overline{T}_z$, net surface heat flux. Contour interval: 0.25 W m^{-2} (std dev)$^{-1}$. Negative contours are dashed, the zero contour is omitted.

spatial map of the surface heat flux in Fig. 10 has a very similar structure to its interannual counterpart, showing strong cooling along the equator, and poleward broadening of positive heat content anomalies in the eastern Pacific. Figure 9b shows that the relative role of each of the dynamic terms differs quantitatively from its respective role on interannual timescales. The $-w'\overline{T}_z$ term largely balances the surface heat flux, and is more than twice the amplitude of the $-u'\overline{T}_x$ and $-\overline{w}T'_z$ terms. Furthermore, the $-w'\overline{T}_z$ term does not contribute to the decay of HC anomalies at the surface or at depth (Figs. 9b and 9c). Despite differences in the relative roles of the dynamical HC tendency terms, spatial maps of these terms in Fig. 10 are nearly identical to the interannual maps of the same terms in Fig. 6, suggesting that the same mechanisms are acting at the surface for both timescales. It should be noted that the $-\overline{v}T'_y$ term (not shown) acts to weakly cool the upper level along the equator due to a weak mean northward flow across the equator (see Vimont 2000). Poleward of about 3°S–3°N this term is positive, implying a net tropical warming by the $-\overline{v}T'_y$ term, and consistent with mean surface divergence away from the equator.

As is the case for the upper level, the dominant terms that balance the lower-level equatorial HC tendency on the decadal timescale (Fig. 9c) are the same as those that act to balance the HC tendency on the interannual timescale. The storage tendency term is balanced by the $-w'\overline{T}_z$, $-\overline{w}T'_z$, and $-u'\overline{T}_x$ terms. The $-w'\overline{T}_z$ term dominates the lower-level HC tendency on decadal timescales. As is true for the interannual timescale, the magnitude of the $-w'\overline{T}_z$ term is about twice that of any of the other terms. Similarly, the spatial structure of the $-w'\overline{T}_z$ term (Fig. 10) shows a very similar structure to the interannual $-w'\overline{T}_z$ term (Fig. 6), though features in the decadal term are meridionally broader than those in the interannual map. Unlike the interannual timescale, the $-w'\overline{T}_z$ term peaks contemporaneously with the lower-level heat content anomaly (cf. Figs. 5a and 5c with Figs. 9a and 9c). Furthermore, the $-w'\overline{T}_z$ term does not act to cool at depth until the surface wind stress and K_f have completely vanished, suggesting that the possible role of delayed upwelling signals along the equator is subdued or absent on decadal timescales.

To further investigate the apparent differences between the interannual and decadal $-w'\overline{T}_z$ terms, spatial maps of the $-w'\overline{T}_z$ term in the lower level during the development, peak, and decay of equatorial HC anomalies are plotted for interannual and decadal timescales in Fig. 11. During the development of an event (lag −1 and lag −4 for the interannual and decadal timescale, respectively), the $-w'\overline{T}_z$ term has very similar spatial structure along the equator for both timescales. However, anomalous upwelling in the western subtropical Pacific for the decadal timescale is much weaker and centered slightly poleward, compared to the upwelling region for the interannual timescale. Assuming this upwelling is caused by westward-propagating Rossby signals, the poleward shift will decrease the efficiency with which the westward-propagating Rossby signals reflect off the western boundary as Kelvin signals (Clarke 1983). Hence, it is not surprising that the spatial structure of the interannual $-w'\overline{T}_z$ term differs significantly from that of the decadal $-w'\overline{T}_z$ term at the peak of equatorial HC anomalies (lag 0 and lag −1, respectively): in the interannual map (lag 0), anomalous downwelling in the central equatorial Pacific is centered in two off-equatorial lobes, while the western Pacific is characterized by strong upwelling. Figure 5 shows that on the interannual timescale, westerly zonal wind stress and K_f have strengthened along the equator, suggesting that downwelling in the central Pacific might also increase. However, Fig. 5 (lag 0) clearly shows a cessation of downwelling anomalies at this time, which, when combined with the spatial structure of upwelling at lag 0 in Fig. 11, is seen to be caused by the dominance of upwelling Kelvin signals (issued from the western boundary reflection) arriving in the central Pacific. The

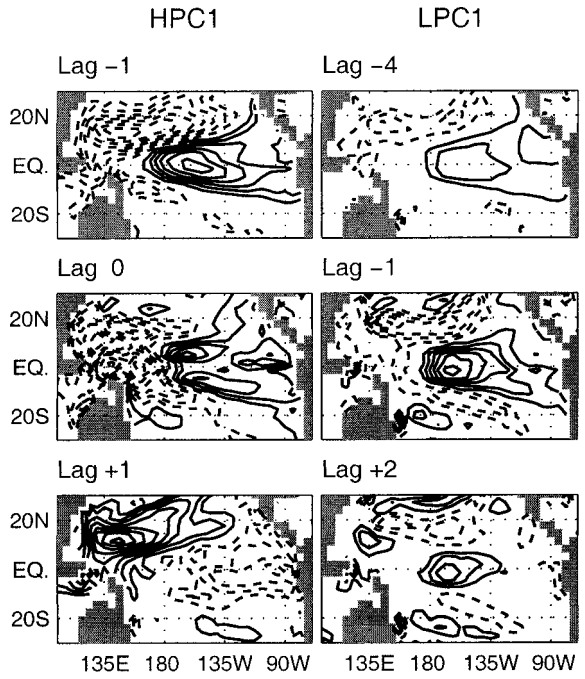

FIG. 11. Lagged regression of the lower-level $-w'\overline{T}_z$ term onto HPC1 (left) and LPC1 (right), for lags corresponding to the development (top), peak (middle), and decay (bottom) of equatorial HC anomalies. Lags −1, 0, and +1 yr are shown for HPC1, and lag −4, −1, and +2 yr are shown for LPC1. Contour interval 0.65 W m^{-2} (std dev)$^{-1}$. Negative contours are dashed, the zero contour is omitted.

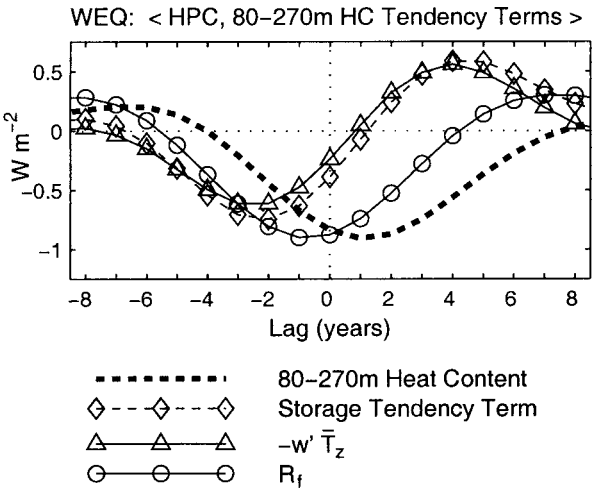

FIG. 12. Lagged regression of annually averaged western equatorial Pacific (10°S–10°N, 120°–165°E) lower-level heat content (scaled), and heat content tendency terms (W m^{-2}) onto LPC1. Also shown is the Rossby wave forcing term, R_f (see text).

arrival of these signals confirms the existence of the negative ocean memory feedback on interannual timescales.

In contrast to the interannual event, Fig. 9 shows that upwelling in the central Pacific for the decadal timescale amplifies with increasing zonal wind stress and K_f, consistent with the local positive Bjerkness feedback associated with coupled dynamics. During the decay of equatorial HC anomalies, the role of the $-w'\overline{T}_z$ term for interannual timescales is opposite that for decadal timescales; for interannual timescales upwelling by $-w'\overline{T}_z$ term acts to decrease the positive HC anomalies in the central and eastern equatorial Pacific and terminate the surface warming, while on decadal timescales, positive zonal wind stress anomalies (and hence positive K_f) still cause anomalous downwelling (and hence warming) in the central equatorial Pacific as the SST (upper-level heat content) is decreasing. For decadal timescales, downwelling in the central Pacific continues until the zonal wind stress vanishes, confirming that the role of the negative ocean memory feedback is subdued, or not operating on the decadal timescale.

The remaining important dynamic terms at depth (Fig. 9c) include the $-\overline{w}T'_z$, and $-u'\overline{T}_x$ terms, which both act to weakly counter the effect of the $-w'\overline{T}_z$ term. The spatial maps of the decadal $-\overline{w}T'_z$ and $-u'\overline{T}_x$ terms during the development phase (Fig. 10) are quite similar to their interannual counterparts, and are explained using similar reasoning. Figure 9c shows that the $-u'\overline{T}_x$ term quickly acts to damp warm anomalies at depth along the equator, though Fig. 10 shows two regions of warming on either side of the equator that are consistent with Rossby wave reflection off the eastern boundary. The broad meridional scale, and wedged shape of the $-u'\overline{T}_x$ and $-\overline{w}T'_z$ terms are consistent with low-frequency equatorial Rossby wave dynamics. By lag −2 the $-u'\overline{T}_x$ term has started cooling the lower-level equatorial region due to a slowing of the equatorial undercurrent (see Fig. 9). This effect contributes to the decay of an event. It is noted that the $-\overline{u}T'_x$ term (not shown) also weakly assists in the decay of an event, though it does not contribute significantly to the development of the following event, as hypothesized by Gu and Philander (1997).

The heat content tendency terms for the western tropical Pacific (averaged over the region 10°S–10°N, 120°–165°E) are plotted in Fig. 12. As for the interannual timescale (Fig. 7), the dominant term in this region is the $-w'\overline{T}_z$ term, which explains nearly all of the storage tendency term. Unlike the interannual timescale, the $-w'\overline{T}_z$ term is not consistent with the Rossby wave forcing term R_f. Note that after lag +1, the $-w'\overline{T}_z$ term begins to *warm* the western equatorial Pacific, while the Rossby wave forcing term suggests that it should cool. This discrepancy between $-w'\overline{T}_z$ and R_f may result from the arrival of downwelling Rossby signals emanating from the eastern boundary, or from some other external process. In either case, the lack of strong anomalous upwelling in the western tropical Pacific adds further evidence that the negative feedback associated with Rossby signals that reflect off the western boundary is subdued or absent for the decadal timescale.

b. Physics of the decadal ENSO-like variability

The preceding equatorial heat budget analysis confirms that the same positive Bjerkness feedback exists for both the interannual and decadal timescale. This positive feedback ensures that coupled tropical ocean basin adjustment will dominate the evolution of heat content anomalies in a similar fashion for both timescales. The broadened meridional structure of the decadal heat content anomalies is completely consistent with the dynamics of low-frequency equatorial waves, and hence with low-frequency basin adjustment.

In contrast to the interannual timescale, the negative ocean memory feedback is subdued, or does not exist for the decadal timescale. The structure of the $-w'\overline{T}_z$ term in the central and western tropical Pacific is found to be qualitatively consistent with the lack of a significant negative ocean memory feedback. To investigate the origin of the differing role of the negative ocean memory feedback between decadal and interannual timescales, the ratio of the Rossby wave forcing term R_f to the Kelvin wave forcing term K_f (R_f/K_f) is examined. Recall that the Rossby wave forcing term is defined to give the (nondimensional) amplitude of a Kelvin wave after a perfect reflection of the first four symmetric Rossby waves off the western boundary. Thus, the ratio R_f/K_f provides an estimate of the ratio of the wave-induced negative feedback to the local positive feedback. The ratio R_f/K_f is -0.44 for interannual timescales, and -0.31 for decadal timescales. Thus the negative ocean memory feedback (or equivalently the western boundary reflection) for the decadal timescale is only 70% as efficient as the interannual timescale.[8] Thus, it is likely that the different wind stress structure on interannual and decadal timescales (and hence, the different amplitude of R_f) partially explains the longer timescales of decadal variability.

c. Interdecadal variability

In section 3, a 25-yr spectral peak is found to be distinguishable from the best-fit AR2 null hypothesis at the 95% level. This same peak is found by Walland et al. (2000) and Cai and Whetton (2001) in similarly constructed time indices. Cai and Whetton (2001) investigate the tropical Pacific response to increased greenhouse gas concentrations in three transient greenhouse warming simulations of the CSIRO CGCM. They provide evidence that in the greenhouse warming scenario, temperature anomalies subduct in midlatitudes, are advected equatorward and westward at depth, and reemerge in the Tropics, similar to the ocean model results of Liu et al. (1994). They go on to speculate that the same mechanism governs interdecadal variability in the same control simulation analyzed in this study. Specifically, based on 15–30-yr bandpass-filtered temperature data from the coupled simulation used in this study, Cai and Whetton (2001) show that surface temperature anomalies in the eastern equatorial Pacific are preceded by subsurface temperature anomalies at depth in the western subtropical Pacific, and hypothesize that the subtropical anomalies in the control simulation originate from subducted temperature anomalies in the midlatitudes.[9]

To determine the cause of the subtropical subsurface temperature anomalies, we repeated the analysis in sections 4a and 5a on the 15–30-yr bandpass-filtered variability. Consistent with the analysis of Vimont (2000), we found that cooling in the subsurface western subtropical Pacific is dominated by locally forced anomalous upwelling, and meridional velocities (the $-w'\overline{T}_z$ and $-v'\overline{T}_y$ terms, respectively). Thus, consistent with Schneider et al. (1999) and Pierce et al. (2000), we conclude that the subsurface western off-equatorial Pacific temperature anomalies are mostly locally forced, consistent with coupled basin adjustment processes. Advection of temperature anomalies (via the $-\overline{u}T'_x$, $-\overline{v}T'_y$, and $-\overline{w}T'_z$ terms) is small in comparison to these locally forced signals. These results do not necessarily rule out a role for advection of temperature anomalies from the midlatitudes in setting the timing of the 25-yr periodicity, but do suggest that sensitivity studies will be required to clarify the underlying mechanism of the periodicity.

6. Discussion

We have analyzed the structure of, and mechanisms responsible for, interannual and decadal variability in the Pacific Ocean that is simulated by the CSIRO coupled general circulation model. Based on EOF analysis of 0–270-m upper-ocean heat content, the leading mode of Pacific variability is shown to be dominated by changes in the Tropics that resemble observations of ENSO (interannual) and ENSO-like (decadal) variability. The spatial structure of modeled interannual and decadal variability closely resemble observations, especially in the Southern Hemisphere. The temporal structure of modeled variability (inferred from spectral analysis of the

[8] The nondimensional, linearized delayed oscillator model for ENSO may be written (Schopf and Suarez 1988; Battisti and Hirst 1989; Neelin et al. 1998):

$$\frac{dT'}{dt} = (c_1K_f - 1)T' - c_2R_fT'(t - \delta). \quad (2)$$

A decrease in R_f implies a decreased negative ocean memory feedback, and hence, a decrease in the frequency of the oscillation (Battisti and Hirst 1989).

[9] The apparent subduction, and equatorward advection of subsurface temperature anomalies may be inferred by examining the development of a warm event in Fig. 8. From lag -3 to lag $+3$, negative lower-level heat content anomalies appear at depth in midlatitudes (near 25°N, 170°W), and in the off-equatorial western tropical Pacific (near 15°N, 135°E). [Similar features appear at interannual timescales (cf. Fig. 4).]

CT index and the first PC of 0–270-m heat content) is best described as an AR2 process with a preferred periodicity of 6–10 yr. Though the temporal structure indicates the modeled interannual variance is weaker than observed, the agreement between the spatial characteristics of modeled variability (both interannual and decadal) and observations suggests that the model may be correctly reproducing mechanisms responsible for the variability.

The evolution of, and mechanisms responsible for, modeled interannual variability are consistent with the so-called delayed oscillator model of ENSO. Like the real world, equatorial westerly wind stress anomalies force eastward-propagating, downwelling thermocline signals. As the thermocline deepens and anomalous eastward currents develop, the surface warms, which feeds back positively on the westerly wind stress anomalies; this is the positive ''Bjerkness'' feedback. At the same time, the westerly wind stress anomalies force upwelling Rossby signals that propagate freely in the western tropical Pacific, reflect off the western boundary, and ultimately counter the local positive feedback in the central Pacific. This is the negative ''ocean memory'' feedback.

The lack of a strong interannual spectral peak in the power spectra of the CT index and PC1 does not preclude realistic dynamics governing the modeled interannual variability. In fact, the agreement between the CT spectrum and the best-fit AR2 null hypothesis (cf. Fig. 2) is entirely consistent with the delayed oscillator physics shown in section 4. To further motivate the use of an AR2 null hypothesis, we investigate the temporal behavior of the CT index produced by a different model, in which the delayed oscillator mechanism is known to produce tropical variability. We use the CT index produced by the Battisti (1988) version of the Zebiak and Cane (1987) intermediate coupled model (ICM), in which certain model parameters have been adjusted to more ''realistic'' values, and stochastic forcing has been added.[10] A 100 000-yr CT index is output by the model, from which the power spectrum is computed, and shown in Fig. 13, as well as the best-fit AR2 spectrum, and 95% and 99% confidence ratios. Note that the plotting convention is the same as that used in Fig. 2, which produces a visual maximum at the inferred periodic timescale of the theoretical AR2 spectrum.

Figure 13 shows that the spectrum of the CT index from the ICM is nearly indistinguishable from the best-fit AR2 null hypothesis at interannual and decadal timescales. Furthermore, the 3.76-yr implied periodicity of the best-fit AR2 null hypothesis is very close to the peak of the spectrum associated with the leading Floquet mode (the ENSO mode) of the coupled system, as well as observations (3.85 and 3.5 yr, respectively; see Thompson and Battisti 2000). The discrepancy between the 3.76-yr periodicity implied in the ICM's CT index, and the 6–10-yr periodicity implied in the CSIRO CGCM's CT index may be explained by excessive damping in the CSIRO coupled simulation. In fact, Thompson and Battisti (2000) find that, by increasing damping in a linearized version of the ICM used here, the interannual spectral peak of the ENSO mode shifts to lower frequencies, and broadens considerably. The longer periodicity in the CSIRO CGCM is consistent with excessive damping in the ocean model, which results in part from the coarse ocean model resolution (see Ng and Hsieh 1994).

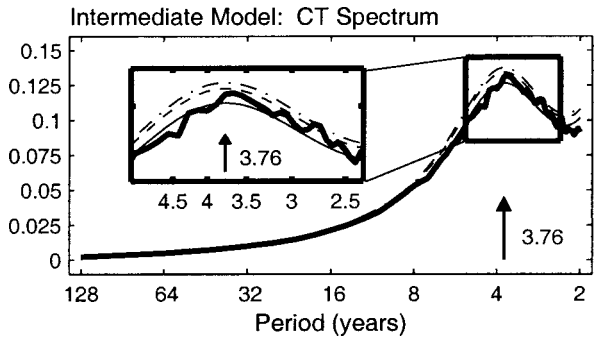

FIG. 13. Power spectrum of the Battisti (1988) intermediate coupled tropical atmosphere–ocean model's CT index (dark solid line), shown together with the best-fit theoretical AR2 spectrum (thin solid line), and the 95% and 99% confidence ratios (thin dashed and dot–dashed lines, respectively). The product of frequency and variance is plotted against the natural log of frequency. The arrow indicates the periodic timescale implied by the theoretical AR2 spectrum: 3.76 yr.

Modeled decadal variability evolves in a very similar manner as the modeled interannual variability. Examination of the mechanisms responsible for decadal variability confirms that the local positive feedback between zonal wind stress, thermocline depth, and SST exists on decadal timescales, as well as interannual, which explains the similar spatial structure of interannual and decadal variability. As hypothesized by Zhang et al. (1997), the meridionally broadened SST and HC anomalies on decadal timescales are consistent with low-frequency equatorial wave dynamics (see Vimont 2000, for a more detailed analysis). In contrast to interannual timescales, however, there is little evidence of a negative ocean memory feedback associated with a western boundary reflection on decadal timescales. Instead, modeled decadal variability damps by numerous processes, including the surface heat flux, and advection by the mean and anomalous equatorial undercurrent. The weakness of the negative ocean memory feedback on decadal timescales may be partially explained by the different structure of interannual and decadal zonal wind stress anomalies equatorward of about 20° latitude.

The subdued negative ocean memory feedback on decadal timescales begs the question, ''is there a specific timescale at which the negative ocean memory feedback ceases to operate'' (T. Knutson 2001, personal com-

[10] A more complete description of the model can be found in Battisti (1988). The present version of the ICM is programmed with the T.80 parameter set of Thompson and Battisti (2000), which produces a damped ENSO Floquet mode that is maintained by stochastic forcing.

munication). For instance, Knutson and Manabe (1998) state that the delayed ocean memory feedback does act in their model on timescales longer than 7 yr. We speculate that the reduction in efficiency of the negative ocean memory feedback is probably a gradual function of timescale, and probably also model dependent.

The results of this study indicate that the bulk of equatorial variability in the CSIRO model is caused by the same mechanism on interannual and decadal timescales. This mechanism is simply the coupled adjustment of the tropical atmosphere–ocean system. Because the coupled adjustment involves the positive Bjerkness feedback, any persistent (longer than the adjustment timescale of the atmosphere) perturbation to the system will excite the same positive feedback, and the basin will adjust in the same manner. As a result, it will be difficult to distinguish the structure and origin of the original perturbation from the structure of the coupled adjustment. This was found to be true for the weak, but statistically significant 25-yr peak in the spectrum of the CT index, and of PC1 (see Fig. 2). In this respect, it seems that sensitivity studies will be essential to determine the mechanism causing the spectral peak at 25 yr.

From this analysis, the different structure of interannual and decadal tropical zonal wind stress anomalies can only be speculated upon. One hypothesis in the literature states that wind stress changes in the Tropics are caused by atmospheric variability in the midlatitudes (Barnett et al. 1999; Pierce et al. 2000; Vimont 2000). According to this hypothesis, internally generated midlatitude atmospheric variability projects zonal wind stress anomalies into the Tropics. The thermocline responds to these wind stress anomalies, producing an ENSO-like, hemispherically symmetric pattern of variability. This latter mechanism appears to be relevant to the decadal variability simulated by the CSIRO CGCM examined herein (Vimont et al. 2001).

Acknowledgments. Special thanks to E. S. Sarachik and J. M. Wallace at the University of Washington for their suggestions and guidance. Comments on the original manuscript by W. Cai, T. Knutson, and S.-P Xie are greatly appreciated. Thanks also to M. Collier for preparing and providing the model data. This work was supported by a grant from the NOAA/Office of Global Programs to the Stanley P. Hayes Center at the University of Washington. This publication was funded by the Joint Institute for the Study of the Atmosphere and Ocean (JISAO) under NOAA Cooperative Agreement NA67RJO155.

REFERENCES

Barnett, T. P., D. W. Pierce, M. Latif, D. Dommenget, and R. Saravanan, 1999: Interdecadal interactions between the tropics and midlatitudes in the Pacific basin. *Geophys. Res. Lett.,* **26,** 615–618.

Battisti, D. S., 1988: Dynamics and thermodynamics of a warming event in a coupled tropical atmosphere–ocean model. *J. Atmos. Sci.,* **45,** 2889–2919.

——, and A. C. Hirst, 1989: Interannual variability in a tropical atmosphere–ocean model: Influence of the basic state, ocean geomentry, and nonlinearity. *J. Atmos. Sci.,* **46,** 1687–1712.

——, and E. Sarachik, 1995: Understanding and predicting ENSO. *Rev. Geophys.,* **33,** 1367–1376.

Cai, W., and P. H. Whetton, 2001: A time-varying greenhouse warming pattern and the tropical–extratropical circulation linkage in the Pacific Ocean. *J. Climate,* **14,** 3337–3355.

Chang, P., L. Ji, H. Li, and M. Flügel, 1996: Chaotic dynamics versus stochastic processes in El Niño–Southern Oscillation in coupled ocean–atmosphere models. *Physica D,* **98,** 301–320.

Clarke, A. J., 1983: The reflection of equatorial waves from oceanic boundaries. *J. Phys. Oceanogr.,* **13,** 1193–1207.

Cox, M. D., 1984: A primitive equation, 3-dimensional model of the ocean. GFDL Ocean Group Tech. Rep. 1, GFDL–Princeton University, Princeton, NJ, 141 pp. [Available from NOAA/Geophysical Fluid Dynamics Laboratory, Princeton University, Princeton, NJ 08542.]

Davis, R. E., and Coauthors, 2000: Implementing the Pacific Basin Extended Climate Study (PBECS). U.S. CLIVAR Office, 123 pp.

Deser, C., 1989: Meteorological characteristics of the El Niño/Southern Oscillation phenomenon. Ph.D. thesis, University of Washington, Seattle, WA, 195 pp.

——, M. A. Alexander, and M. S. Timlin, 1996: Upper-ocean thermal variations in the North Pacific during 1970–1991. *J. Climate,* **9,** 1840–1855.

Fletcher, J. O., R. J. Slutz, and S. D. Woodruff, 1983: Towards a comprehensive ocean–atmosphere dataset. *Trop. Ocean–Atmos. Newsl.,* **20,** 13–14.

Frankignoul, C., P. Müller, and E. Zorita, 1997: A simple model of the decadal response of the ocean to stochastic wind forcing. *J. Phys. Oceanogr.,* **27,** 1533–1546.

Gargett, A. E., 1984: Vertical eddy diffusivity in the ocean interior. *J. Mar. Res.,* **42,** 359–393.

Garreaud, R. D., and D. S. Battisti, 1999: Interannual (ENSO) and interdecadal (ENSO-like) variability in the Southern Hemisphere tropospheric circulation. *J. Climate,* **12,** 2113–2123.

Gent, P. R., and J. C. McWilliams, 1990: Isopycnal mixing in ocean circulation models. *J. Phys. Oceanogr.,* **20,** 150–155.

Gordon, H. B., and S. P. O'Farrell, 1997: Transient climate change in the CSIRO coupled model with dynamic sea ice. *Mon. Wea. Rev.,* **125,** 875–907.

Gu, D., and S. G. H. Philander, 1997: Interdecadal climate fluctuations that depend on exchanges between the tropics and extratropics. *Science,* **275,** 805–807.

Hirst, A. C., S. P. O'Farrell, and H. B. Gordon, 2000: Comparison of a coupled ocean–atmosphere model with and without oceanic eddy-induced advection. Part I: Ocean spinup and control integrations. *J. Climate,* **13,** 139–163.

Kawamura, R., 1994: A rotated EOF analysis of global sea surface temperature variability with interannual and interdecadal scales. *J. Phys. Oceanogr.,* **24,** 707–715.

Kirtman, B. P., 1997: Oceanic Rossby wave dynamics and the ENSO period in a coupled model. *J. Climate,* **10,** 1690–1705.

Kitoh, A., T. Motoi, and H. Koide, 1999: SST variability and its mechanism in a coupled atmosphere–mixed layer ocean model. *J. Climate,* **12,** 1221–1239.

Knutson, T. R., and S. Manabe, 1998: Model assessment of decadal variability and trends in the tropical Pacific Ocean. *J. Climate,* **11,** 2273–2296.

——, ——, and D. Gu, 1997: Simulated ENSO in a global coupled ocean–atmosphere model: Multidecadal amplitude modulation and CO_2 sensitivity. *J. Climate,* **10,** 138–161.

Latif, M., 1998: Dynamics of interdecadal variability in coupled ocean–atmosphere models. *J. Climate,* **11,** 602–624.

Lau, K.-M., and H. Weng, 1999: Interannual, decadal–interdecadal,

and global warming signals in sea surface temperature during 1955–97. *J. Climate*, **12,** 1257–1267.

Liu, Z., S. G. H. Philander, and R. C. Pacanowski, 1994: A GCM study of tropical-subtropical upper-ocean water exchange. *J. Phys. Oceanogr.*, **24,** 2602–2623.

Lysne, J., P. Chang, and B. Giese, 1997: Impact of the extratropical Pacific on equatorial variability. *Geophys. Res. Lett.*, **24,** 2589–2592.

Mantua, N. J., and D. S. Battisti, 1994: Evidence for the delayed oscillator mechanism for ENSO: The ''observed'' oceanic Kelvin mode in the far western Pacific. *J. Phys. Oceanogr.*, **24,** 691–699.

——, S. R. Hare, Y. Zhang, J. M. Wallace, and R. C. Francis, 1997: A Pacific interdecadal climate oscillation with impacts on salmon production. *Bull. Amer. Meteor. Soc.*, **78,** 1069–1079.

McCreary, J. P., 1983: Model of tropical ocean–atmosphere interaction. *Mon. Wea. Rev.*, **111,** 370–387.

Moore, A. M., 1995: Tropical interannual variability in a global coupled GCM: Sensitivity to mean climate state. *J. Climate*, **8,** 807–828.

Neelin, J. D., D. S. Battisti, A. C. Hirst, F. Jin, Y. Wakata, T. Yamagata, and S. E. Zebiak, 1998: ENSO theory. *J. Geophys. Res.*, **103** (C7), 14 261–14 290.

Ng, M. K. F., and W. W. Hsieh, 1994: The equatorial Kelvin wave in finite difference models. *J. Geophys. Res.*, **99,** 14 173–14 185.

Nonaka, M., S.-P. Xie, and K. Takeuchi, 1999: Equatorward spreading of a passive tracer with application to North Pacific interdecadal temperature variations. *J. Oceanogr.*, **56,** 173–183.

O'Farrell, S. P., 1998: Sensitivity study of a dynamical sea ice model: The effect of the external stresses and land boundary conditions on ice thickness distribution. *J. Geophys. Res.*, **103,** 15 751–15 782.

Pierce, D. W., T. P. Barnett, and M. Latif, 2000: Connections between the Pacific Ocean Tropics and midlatitudes on decadal timescales. *J. Climate*, **13,** 1173–1194.

Schneider, N., S. Venzke, A. J. Miller, D. W. Pierce, T. P. Barnett, C. Deser, and M. Latif, 1999: Pacific thermocline bridge revisited. *Geophys. Res. Lett.*, **26,** 1329–1322.

——, A. J. Miller, and D. W. Pierce, 2002: Anatomy of North Pacific decadal variability. *J. Climate*, in press.

Schopf, P. S., and M. J. Suarez, 1988: Vacillations in a coupled ocean–atmosphere model. *J. Atmos. Sci.*, **45,** 549–566.

Suarez, M. J., and P. S. Schopf, 1988: A delayed action oscillator for ENSO. *J. Atmos. Sci.*, **45,** 3283–3287.

Tett, S., 1995: Simulation of El Niño–Southern Oscillation-like variability in a global AOGCM and its response to CO_2 increase. *J. Climate*, **8,** 1473–1502.

Thompson, C. J., and D. S. Battisti, 2001: A linear stochastic dynamical model of ENSO. Part II: Analysis. *J. Climate*, **14,** 445–466.

Timmermann, A., M. Latif, A. Grötzner, and R. Voss, 1999: Modes of climate variability as simulated by a coupled general circulation model. Part I: ENSO-like climate variability and its low-frequency modulation. *Climate Dyn.*, **15,** 605–618.

Vimont, D. J., 2000: Pacific interannual to interdecadal variability in the CSIRO coupled general circulation model. M.S. thesis, Dept. of Atmospheric Sciences, University of Washington, 154 pp.

——, D. S. Battisti, and A. C. Hirst, 2001: Footprinting: A seasonal link between the mid-latitudes and tropics. *Geophys. Res. Lett.*, **28,** 3923–3926.

von Storch, H., and F. W. Zwiers, 1999: *Statistical Analysis in Climate Research.* Cambridge University Press, 484 pp.

Wakata, Y., and E. S. Sarachik, 1992: Effects of the meridional extent of mean equatorial upwelling on atmosphere–ocean coupled instabilities over an unbounded ocean. *J. Meteor. Soc. Japan*, **70,** 843–854.

Walker, G. T., and E. W. Bliss, 1932: World weather V. *Mem. Roy. Meteor. Soc.*, **4** (36), 29–64.

Wallace, J. M., E. M. Rasmusson, T. P. Mitchell, V. E. Kousky, E. S. Sarachik, and H. von Storch, 1998: On the structure and evolution of ENSO-related climate variability in the tropical Pacific: Lessons from TOGA. *J. Geophys. Res.*, **103,** 14 241–14 259.

Walland, D. J., S. B. Power, and A. C. Hirst, 2000: Decadal climate variability simulated in a coupled general circulation model. *Climate Dyn.*, **16,** 201–211.

Xie, S.-P., T. Kunitani, A. Kubokawa, M. Nonaka, and S. Hosoda, 2000: Interdecadal thermocline variability in the North Pacific for 1958–97: A GCM simulation. *J. Phys. Oceanogr.*, **30,** 2798–2813.

Yukimoto, S., M. Endoh, Y. Kitamura, A. Kitoh, T. Motoi, A. Noda, and T. Tokioka, 1996: Interannual and interdecadal variabilities in the Pacific. *Climate Dyn.*, **12,** 667–683.

Zebiak, S. E., 1985: Tropical atmosphere–ocean interactino and the El Niño/Southern Oscillation phenomenon. Ph.D. thesis, Massachusetts Institute of Technology, 261 pp.

——, and M. A. Cane, 1987: A model ENSO. *Mon. Wea. Rev.*, **115,** 2262–2278.

Zhang, Y., J. M. Wallace, and D. S. Battisti, 1997: ENSO-like interdecadal variability: 1900–93. *J. Climate*, **10,** 1004–1020.